Development of a software framework to assess the potential of adaptive trailing edge flaps on horizontal-axis wind turbines

Department of Wind Energy Master Report

Rogier Roderick Vossebeld

DTU Wind Energy-M-0330

July 2019

DTU Wind Energy
Department of Wind Energy

Author: Rogier Roderick Vossebeld

Title: Development of a software framework to assess the potential of adaptive trailing edge flaps on horizontal-axis wind turbines

DTU Wind Energy-M-0330July 2019

Project period:
November 2018 – July 2019

ECTS: 45

Education: Master of Science

Supervisors:

Mac Gaunaa
DTU Wind Energy

Carlos Simao Ferreira
TU Delft

Stefan Kneissl
Enercon

Remarks:
This report is submitted as partial fulfillment of the requirements for graduation in the above education at the Technical University of Denmark.

DTU Wind Energy is a department of the Technical University of Denmark with a unique integration of research, education, innovation and public/private sector consulting in the field of wind energy. Our activities develop new opportunities and technology for the global and Danish exploitation of wind energy. Research focuses on key technical-scientific fields, which are central for the development, innovation and use of wind energy and provides the basis for advanced education at the education.

We have more than 240 staff members of which approximately 60 are PhD students. Research is conducted within nine research programmes organized into three main topics: Wind energy systems, Wind turbine technology and Basics for wind energy.

Technical University of Denmark
Department of Wind Energy
Frederiksborgvej 399
4000 Roskilde
Denmark

www.vindenergi.dtu.dk

Development of a software framework to assess the potential of adaptive trailing edge flaps on horizontal-axis wind turbines

by

R.R. Vossebeld

to obtain the degree of Master of Science
at the Delft University of Technology, and at the Technical University of Denmark,
to be defended publicly on Tuesday August 13, 2019 at 10:00 AM.

Student number TU Delft:	4277287	
Student number DTU:	171705	
Project duration:	November 1, 2018 – July 31, 2019	
Thesis committee:	Dr. C. S. Ferreira,	TU Delft, academic supervisor
	Dr. M. Gaunaa,	DTU, academic supervisor
	Dr. S. Bott,	ENERCON WRD, supervisor

TU Delft

Acknowledgements

With thanks to my supervisors; Carlos, to you I owe having started as a student in the EWEM programme, by your words that were key in my decision to apply. I could not have wished for a better MSc education, it has been a very rewarding experience. To Mac, with your patience and positive attitude, from gathering all in the first brainstorm session to shape the thesis, to being available for a discussion no matter your whereabouts. To Stefan, who helped me through the rough C++ times at the start and whose calm attitude often relieved the stress from the situation. To Stefanie, who followed the thesis with interest from the start and when the need presented itself, kindly took the role as the company supervisor on her.

To the people at Enercon, whose company, both during the long hours and of course the leisure times, made the stay in the remote Aurich to a pleasant experience.

Last but not least, a thank you to my family, friends and close ones, for the cheerful times and the support throughout.

R.R. Vossebeld
Aurich, July 2019

Contents

1 Introduction

Over the recent years, the size of HAWTs has grown as a result of the endeavours to generate more wind energy, at a lower LCOE. Over time this has resulted in larger rotor sizes with higher power output, introducing the challenge of dealing with the consequent increase in loads, for which mitigation strategies can involve both passive and active load control.

A highly promising active load attenuation technique is the ATEF as has been shown by research over the past years, with an early presentation of the potential fatigue load reduction benefits in [28] and an extensive, more recent treatment of the matter in the book [5], based on the PhD dissertation [4]. The use of ATEFs on wind turbine blades is still in a research stage with limited full-scale applications such as presented in [11] and the thesis therefore aims at developing a framework that can be used to perform servo-aero-elastic simulations on different wind turbines and different load cases, including the effects of ATEFs to deepen the academic understanding of these active load control devices and accelerate the development thereof in industry.

The MSc thesis project is about the investigation of the possible benefits of the implementation of an Adaptive Trailing Edge Flap (ATEF) on the blades of a Horizontal-Axis Wind Turbine (HAWT). The ATEF can be used to actively attenuate loads on a wind turbine such as fatigue- and peak loads. In order to model this, a dynamic stall model will be coupled to the in-house BEM-based Enercon software, and extended with a dynamic inflow model, to create a framework which combined with a control strategy allows for performing aero-servo-elastic simulations. The dynamic stall model will be based on the literature of the state-of-the-art ATEFlap software module and validated against experimental data from the AVATAR project, in which wind tunnel data on loads induced by unsteady flap oscillations were obtained [10].

Using this framework, the importance of the dynamic models and their effect is shown. Combined, the framework is used to assess the performance of a reference turbine both with and without ATEFs, for the load case: normal operation with extreme turbulence (Design Load Case 1.3 of IEC 61400-1). The turbine in consideration is the Tjaereborg 2 MW turbine, for which validation data of the dynamic inflow model is available. Additionally, investigations on flap placement, actuation speed and load reduction are done to gain an insight in how these affect the (fatigue) loads experienced by the turbine. With ATEFs, the application of active flow control, a well-known concept that has been around since the start of the powered flight, comes within reach for HAWTs, and the expected advantages introduce the possibility to perform a load-neutral upscaling with the use of active flap control. This would aid in reducing the Levelised-Cost-Of-Energy (LCOE) of HAWTs and in turn ameliorate the position of wind energy in the market.

2

Literature review

In this section a brief overview of existing load alleviation techniques and research performed on them is given. As the ATEF technique is the load alleviation treated in this thesis, a background on both the experimental and non-experimental research on this technique is given, and simulation methods treated. Additionally, the dynamic inflow model selected is detailed upon.

2.1. Load alleviation techniques

When load alleviation techniques are treated, a distinction is made between active and passive techniques. Passive load reduction is attained by tailoring the aero-elastic response of the wind turbine blades, such that with increased loading, the corresponding deformation automatically leads to a reduction in loads, without the need for a control system or active actuation. Examples of this are bend-twist coupling as treated in [24], [22]) and passive flaps [8].

In active load alleviation techniques, the shape of the blades or aerodynamic surfaces is actively controlled and used to reduce the loads on the blades by changing either the lift curve (by changing the aerofoil shape) or by changing the angle of attack and thereby the loads by moving over the polar. In [2], an overview of different active load alleviation techniques is given.

In this overview, the different aerodynamic techniques treated are microtabs, active twist, boundary layer control, camber control and ATEFs. Microtabs are small tabs that are deployed on the aerofoil surface to alter the lift coefficient, with changes of up to 0.4 in C_l, but decreasing the lift over drag ratio in the operational region of the aerofoil (before stall). Active twist is due to the need to deform large sections of or the whole blade, high in energy consumption, with low response times, and therefore unattractive for wind turbine applications. Camber control is the general term for devices that change the camber of the aerofoil, and therefore the lift polar of the section. For morphing the whole aerofoil, a compliant mechanism or many actuators are required. Alternatively, by using continuously deformed trailing edges (ATEFs) the camber changing effect can be attained with little actuation. For this type of actuation, the actuation speed needs to be at least twice that of the disturbance to be countered, which needs to be kept in mind as this might be a limiting factor and prevent the theoretical advantageous effect to be reached. ATEFs are, together with other morphing techniques, listed as the most potent techniques in terms of changing the lift coefficient [2]. The importance of continuous variation in the trailing edge flaps is stressed as the classical work [1] has shown for the effectiveness of flaps compared to a flat, hinged flap.

2.2. Adaptive Trailing Edge Flap

The load alleviation technique treated in this thesis is the ATEF, for which a short overview of potential as found by research is given in this section.

2.2.1. Load reduction using ATEF

Research of ATEF has shown considerable advantages in terms of load reduction and AEP maximisation. In [? , Table III], an overview is given of different investigations on the Upwind 5MW reference wind turbine, with reductions in blade root flapwise bending moment found up to 35% and reductions in damage equivalent load (DEL) between 10 and 47.9%. On the NREL 5MW Offshore wind turbine, the work in [?] showed a 20% reduction in blade root flap moment. In [9], a 26% load reduction was found for blade root bending moment, and a 2-3% increase in rotor size, corresponding to a net increase of 1-2% of annual energy production (AEP).

2.2.2. Simulation methods for ATEF

The most exact numerical simulation is DNS (Direct Numerical Simulation), in which the Navier-Stokes equations are resolved up until the Kolmogorov scales, which due to the extremely high computational cost is not a feasible technique. Even though less computationally techniques such as LES (Large Eddy Simulations), RANS (Reynolds Averaged Navier Stokes) and variants thereof exist, due to the need for time-marching simulations, these are all too computationally expensive. This leaves engineering models, based on vortex-methods or on BEM, where BEM has the lowest computational cost. In section 2.3, the physical working principle of BEM and two solving techniques are described.

In order to accurately simulate ATEFs, an aero-servo-elastic framework has to be used, for which an aerodynamic and structural model have to be coupled and combined with a control strategy. The state-of-the-art aerodynamic model that is used in the work of [5] is capable of modelling the effects of ATEFs. This aerodynamic model named ATEFlap, developed for the aeroelastic simulation software HAWC2, models the unsteady dynamics (wake dynamics added mass effects) based on the potential flow work in [28] [14], as well as dynamic stall based on the Beddoes-Leishman model [3][21]. Worth noting is that next to HAWC2, this model is also implemented in the aeroelastic software DU-SWAT [6]. The model is based on a potential-flow model described in [14], [13] and combines this with a Beddoes-Leishman type dynamic stall model. Furthermore, the model allows for an implementation in a BEM code. In [20], the ATEFlap model is compared to a Reynolds-Averaged-Navier-Stokes solver and to a viscous-inviscid interaction method and is found to have a computational requirement of about 4000 and 10-15 times less, respectively, whilst being able to deliver accurate results for the unsteady loads. Further theoretical background and functionality of the module are treated in [19] and for this thesis, this work will be used as a guideline to extend the in-house BEM software with an aerodynamic model that has the functionalities of the aforementioned model.

2.2.3. Experimental research on ATEF

Experimental results for ATEFs are not abundant, though several experiments have been performed. In one project, the AdVanced Aerodynamic Tools for lArge Rotors (AVATAR) project, an extensive study on the steady and unsteady performance of a flap-equipped wind turbine aerofoil was executed.

The AVATAR project was carried out in the EU's Seventh Programme for research, technological development and demonstration, advanced aerodynamic models were developed and validated. The goal of this project was to support the development of large scale wind turbines up to 20 MW and make these feasible and cost effective[1]. Part of this project was the generation of validation data for trailing-edge flaps in (WP3: Modeling of Flow Devices and Flow Control, Task 3.1), of which the results are described in [10]. Here, a rigid trailing edge flap equipped DU95W180 aerofoil is evaluated experimentally for steady and unsteady flow conditions in the Low Turbulence Wind Tunnel of Delft University of Technology. In the experiment, the aerofoil is tested in sixty cases with varying conditions: free and forced

[1] https://www.eera-avatar.eu/, accessed on 25/04/2019

transition, varying angle of attack and flap angle, in steady and unsteady conditions.

The results from this project are used to validate the implementation of the ATEFlap aerodynamic model in the thesis work, which is elaborated upon in section 5.2.

2.3. Blade Element Momentum theory

In this section, the fundamentals of Blade Element Momentum theory (BEM), such as described in [29], [16], are briefly covered. Two implementations for solving the BEM equations: the Hansen and the Ning approach are treated.

2.3.1. Actuator disc

A fundamental concept that underlies the BEM method is that of the actuator disc. The actuator disk can be used to describe what happens to the flow passing through a wind turbine in a most simplistic manner, by replacing the wind turbine by a disk. The flow is represented by a streamtube, which due to the slow-down of the flow near the turbine and in the wake causes to expand in maintaining continuity. The slow-down of the flow is represented by the axial induction factor a which, multiplied with the inflow velocity, represents the decreased velocity at the actuator disk. The slowdown of the flow before the actuator disk causes the static atmospheric pressure to rise, which drops at the actuator disk due to the energy being extracted from the flow here. In the recovery of the pressure behind the actuator disk, in the wake, kinetic energy is converted into pressure energy, causing the flow to slow down further until the pressure reaches the level of the surrounding atmospheric pressure. With this concept, upon applying the continuity, momentum and energy equations, the far-wake velocity is shown to be slowed down by twice the decrease seen at the actuator disk, and also elementary expressions for power and thrust are obtained as a function of the axial induction parameter a. The power coefficient is given by equation (2.1).

$$C_P = 4a(1-a)^2 \tag{2.1}$$

This equation shows that the physically attainable limit of energy extraction, the well-known Betz limit, lies at $C_{P,max} = 16/27 \approx 0.593$. Considering the far-wake velocity $(1-2a)V_{inflow}$, it is to be noted that the momentum theory yields nonphysical negative wake velocities for a>0.5.

2.3.2. Classical BEM

The classical BEM relies on the actuator disk concept. The actuator disk is sliced up into annular rings around the blade, that are assumed to be radially independent, i.e. not accounting for any radial flow that would arise in a non-uniform radial distribution of a. Additionally, the force applied on the fluid by the blades is assumed to be uniform over a single annular ring, which for a finite number of blades cannot be.

The velocity triangle over the blade is composed of the rotational velocity (tangential) and the inflow velocity (normal) to form the relative inflow velocity vector at the blade element. As in the actuator disk model, the magnitude of the inflow velocity is decreased by the axial induction factor a times the free-stream flow speed. The tangential speed is increased by a factor $a'\omega r$, which is due to the rotational wake velocity perceived by the blade element. The flow angle, the angle between the rotor plane and the relative inflow velocity, comprised of the pitch (θ), twist (β_{twist}) and angle of attack (α), can then be defined as equation (2.2).

$$\phi = \theta + \beta_{twist} + \alpha = \arctan\left(\frac{U_\infty(1-a)}{\omega r(1+a')}\right) \tag{2.2}$$

As soon as the induction factors that define ϕ are found, the values of $C_l(\alpha)$ and $C_d(\alpha)$ are, for a steady BEM computation, obtained from a look-up of the polar data. When these coefficients are known, the desired normal and tangential loads on the blade element can be found.

However, the computation of the induction factors is not that straightforward. Firstly, the losses due to the vorticity shed at the root and tip have to taken into account. This is done by application of

the Prandtl correction. Another correction that is applied is the Glauert correction, used to shape the behaviour of the BEM method in the empirical region where the momentum theory (starts to) break down. Both corrections affect the computation of the axial induction factor, though only the Prandtl correction affects the computation of a'. Additionally, an iterative method is needed to find a solution for a, for which variations exist.

The solving technique as described in [16], is aimed at finding a solution for the axial induction a, using under-relaxation. It is first computed without the Glauert correction, and checks whether a preset cut-off value of a is reached. If so, the axial induction is re-computed using a Glauert-corrected expression.

Another solving technique is described in [26], and iteratively finds a solution for the flow angle ϕ directly, using a root-finding method such as Brent's method. The root-finding algorithm aims to reduce the residual given by equation (2.3), a rewritten form of equation (2.2), until it falls below the set tolerance.

$$\mathcal{R}(\phi) = \frac{\sin(\phi)}{1-a} - \frac{\omega r}{U_\infty}\frac{\cos(\phi)}{1+a'} \tag{2.3}$$

With the solution for the flow angle, together with a non-dimensional parameter incorporating Prandtl's correction, it is determined whether the solution falls in the empirical region or not, and the solution of a depends on the subdivision made into momentum-, empirical- or propeller brake region.

As the classical, steady BEM is incapable of accounting for dynamic effects that arise from changing loads and the corresponding shedding of vorticity, additional alterations and models are required. In this thesis work, the implementation of the ATEFlap aerodynamic model, as well as the Øye dynamic inflow model, both in the Hansen and Ning approach, are treated.

2.4. Dynamic inflow model

The unsteady aerodynamic model on a blade section level (such as the ATEFlap model) captures unsteady aerofoil dynamics. However, in order to capture the effects of the unsteadiness caused by dynamics of the wake development on a rotor level due to changes in loading and the corresponding shedding of vorticity, a dynamic inflow model needs to be implemented. This is also stressed by [25] for model predictive control.

The dynamic inflow model corrects the induced velocities and acts on a timescale much larger than that of unsteady aerofoil aerodynamics [15]. In [27] an extensive comparison of different dynamic inflow models is given. For the axial symmetric case, three engineering models are treated that are implementable in a BEM code, which are all based on the Pitt and Peters model for helicopter applications, an overview of which can be found in [12]. The three models are therefore similar, all adding time derivative terms to the local inflow velocity. One of these models, the Øye model, has been selected for implementation for this thesis work. It incorporates two time scales, fitted to the results of a vortex-ring-wake model, which causes the model to resemble the behaviour observed in such computationally more intensive model, giving it an advantage over the similar models.

3

Research questions, aims and objectives

The main research (sub-)questions of the project are defined to be:

1. What is the importance of dynamic models in ATEF simulation?
    1.1. How well do results produced with the ATEFlap aerodynamic model perform when compared to experimental results?
    1.2. When is the implementation of a dynamic inflow model needed?
    1.3. How do the dynamic inflow model and the ATEFlap aerodynamic model behave when used simultaneously?
2. How do the dynamic models affect the wind turbine performance of a reference wind turbine altered after implementation of ATEFs?
    2.1. How does the flapwise fatigue loading observed in normal operation with atmospheric turbulence change with the presence of ATEFs (NTM, DLC 1.2)?
    2.2. What is the effect of spanwise flap extension on the load-alleviation potential?

These research questions reflect the most important questions that ought to be answered with the use of the software framework, of which the development is the main objective of this work. As for the Tjaereborg wind turbine there is validation data available for the dynamic inflow model, this wind turbine is used to answer the research questions.

The performance during normal operation with normal and extreme turbulence, as described in DLC (Design Load Case) 1.2 and 1.3 of the IEC 61400-1 standard, of the equipped turbine will then be compared to the baseline turbine without ATEFs, allowing for a quantitative and qualitative assessment of the effect of the ATEFs on the fatigue load of the flapwise root bending moment fatigue. With this DLC the performance during normal, power-generating operation is considered. The main aim is to find out how ATEFs can be used to reduce fatigue loads during normal operation and develop a software framework that allows to evaluate the impact of ATEFs on selected wind turbines and load cases.

For research question one, potentially the performance under ultimate load can further be investigated, though the intent of the thesis is to set up the framework for the evaluation of ATEFs on HAWTs, which can then be used to do additional simulations with different wind turbines and different load cases. This is to increase the understanding and accelerate the development of ATEF implementation. It is acknowledged that for a complete analysis and thorough answer to research question two, a multitude of load cases have to be considered.

4

Methodology

The hypothesis is that the ATEFs will considerably reduce the flapwise fatigue load of the turbine blades and when implemented, allow for a load-neutral upscaling of the turbine without compromising the performance otherwise, as indicated by the research presented in [4]. In the current project a software framework consisting of an aerodynamic model with dynamic stall functionality coupled to the in-house BEM software is to be developed, for which the methodology is outlined in this chapter.

4.1. ATEFlap aerodynamic model

The aerodynamic model used is described in [19]. A flowchart of how the ATEFlap aerodynamic model is implemented is shown in figure 4.1.

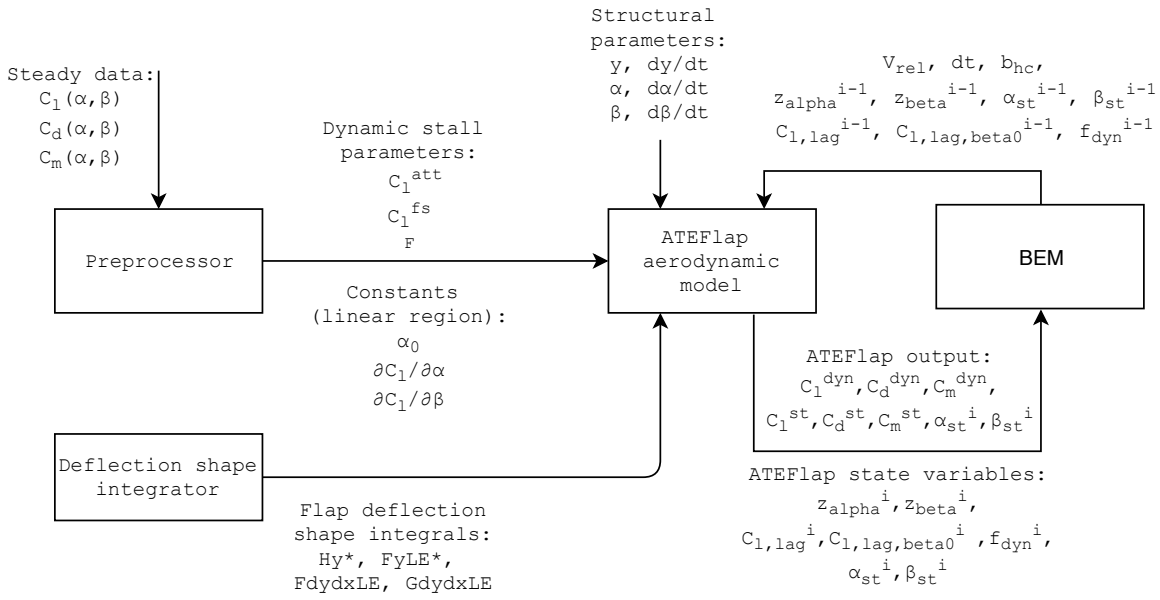

Figure 4.1: Flowchart of the ATEFlap aerodynamic model, including the coupling to BEM.

Here, the steady aerofoil data going into the preprocessor is externally computed, the preprocessor takes this data computes the attached lift coefficient, fully stalled lift coefficient and the stall parameter f that indicates the level of stall at the respective angle of attack and flap angle, as detailed upon in section 4.1.1. These curves are then manually verified and corrected where necessary, as any deviation from the linear attached flow curve is interpreted as stall and can lead to local nonphysical values peaks. As the aerodynamic model is also used for sections without flap to capture dynamic effects induced by

pitch actuation and changing inflow conditions, for these sections the preprocessor is run with dummy data for the flap deflections, to get the dynamic stall parameters for a variation in steady angle of attack.

Next to these dynamic stall parameters, the ATEFlap model requires the deflection shape integrals as specified in [14], the pre-processor computes the required parameters: the attached and fully stalled lift coefficients (by taking the extended linear behaviour and modelling the stalled lift), as well as the f value which describes the extent to which the data shows stall behaviour. Using the inflow and structural parameters supplied by the BEM and elastic code, together with the flap deflection integrals, the ATEFlap model uses the equations in [19] to compute the dynamic lift, drag and moment coefficients.

4.1.1. ATEFlap preprocessor

The preprocessor as shown in the flowchart in figure 4.1, is a tool that needs to be used on the steady aerofoil input data to be used in the aerodynamic model. The preprocessor is described in detail in [19]. Next to the computation of the linear parameters α_0, $\partial C_l/\partial\alpha$, $\partial C_l/\partial\beta$, which are used to compute the linear lift coefficient C_l^{lin} (equation (4.1)), it computes the separation function value $f(\alpha,\beta)$, for which the equation is given by equation (4.2).

$$C_l^{lin} = \frac{\partial C_l}{\partial \alpha}(\alpha - \alpha_0) + \frac{\partial C_l}{\partial \beta}(\beta) \tag{4.1}$$

$$f(\alpha,\beta) = \left(2\sqrt{\frac{C_l^{st}}{C_l^{lin}}} - 1\right)^2 \tag{4.2}$$

The value of f is unity for a fully attached flow, zero for a fully stalled flow, and lies in between these values in the transition region where it acts as a weighting factor between the C_l^{att} and C_l^{fs}, as in equation (4.3).

$$C_l^{st} = C_l^{att} f^{st} + C_l^{fs}(1 - f^{st}) \tag{4.3}$$

The manual check performed on the computation of f is to remove nonphysical peaks or deviations from unity in the attached region. The preprocessor computes the lift coefficient breakdown (C_l^{fs}, C_l^{att}) as follows. The attached lift coefficient is always equal to the linear lift coefficient, except for fully attached flow (here the original steady data input is taken). The fully stalled lift coefficient is taken to be half of the steady value, and in the transition region (for $0 < f < 1$) is given by equation (4.4).

$$C_l^{fs} = \frac{C_l^{st} - C_l^{lin} f^{st}}{1 - f^{st}} \tag{4.4}$$

The preprocessing thus provides the look-up table for all variables needed in the dynamic stall part of the ATEFlap aerodynamic model, as described in the following section. The original Preprocessor for ATEFlap Dynamic Stall model, version 2.05 executable has been used throughout the thesis work, as the pre-processing of the polar data is essential to a correct functioning of the model, and the executable eases the manual corrections needed.

In addition to the format requirements and guidelines in appendix C of [19], it is emphasised that the preprocessor needs input at exactly 0.0 degrees flap angle for the computation of the zero-lift angle of attack and the linear lift slopes for pitch and flap actuation, otherwise preset values will be used without a warning message, which will cause the model to give wrong results for the selected aerofoil, especially in the near-stall region. In the AVATAR validation study, an additional interpolation step of the steady windtunnel data was therefore performed in the preprocessing phase.

4.1.2. Governing ATEFlap equations

The ATEFlap aerodynamic model relies on potential-flow (incompressible), straight-wake and thin-aerofoil assumptions, and discards effects of angular accelerations which for moderate reduced frequencies are deemed negligible. Fundamentally, the basis for unsteady aerofoil aerodynamics for thin aerofoils is laid in the classical work by Theodore Theodorsen [30], also for this model [23].

A multitude of physical effects is modelled by the ATEFlap model. Firstly, the effect of the motion of the aerofoil (heave, pitch- and flap motion) on the angle of attack (α) and flap deflection angle (β) is given by the quasi-steady formulation in equation (4.5) using the small-angle approximation. For β_{qs}, the integral value H_y^*, is one of the deflection shape integrals described in the work by Gaunaa [14]. In this thesis the non-dimensional deflection shape integrals H_y^*, F_y^*, $G_{dy/dx,LE}^*$, $F_{dy/dx,LE}^*$ are used, which are constant values for a given setup, as listed in table 4.1. For the AVATAR validation procedure, the non-dimensional values are calculated with a rigid 0.6 m chord length flap with 0.2 m rigid flap. In the other simulations, a setup with a cusped trailing-edge flap spanning 10% of the chord is used.

Table 4.1: Values for the non-dimensional deflection shape integrals used in the simulations involving the ATEFlap model.

	H_y^*	$F_{y,LE}^*$	$F_{dy/dx,LE}^*$	$G_{dy/dx,LE}^*$
AVATAR validation	-0.0345	0.0138	0.0501	0.0152
Other simulations	-0.0047	0.0004	0.0073	0.0033

$$\alpha_{qs,3/4} = \alpha_{st} - \frac{1}{U_0}\dot{y} + \frac{(0.5 - \epsilon_{ea})c}{2U_0}\dot{\alpha} \tag{4.5}$$

$$\beta_{qs} = \beta - \frac{c}{2U_0}\frac{H_y^*}{\partial C_l/\partial \beta}\dot{\beta} \tag{4.6}$$

The non-circulatory part of the model, which models the added-mass effects caused by the motion of the aerofoil, is instantaneous and for the lift coefficient given by equation (4.8).

$$C_{\ell,nc} = \frac{c}{2V_{rel}}\left(\pi\dot{\alpha} + \frac{cF_{dy/dx,LE}^*}{2\pi}\dot{\beta}\right) \tag{4.7}$$

The potential effect is captured by computation of the effective downwash using the indicial response function Φ, which is an approximation of the Wagner function. If no experimental values for A_i, b_i are known for the aerofoil in consideration, the Jones approximation [18] for a flat plate can be used. In this thesis, the values provided in [19] for the NACA 64-418 aerofoil are used. The time in the expression is the non-dimensional time τ.

$$\Phi = 1 - \sum_{i=1}^{N_{lag}} A_i \exp(b_i\tau), \quad \tau = \frac{U_0 t}{c/2} \tag{4.8}$$

$$\dot{z}_i = \frac{2U_0}{c} b_i (A_i w_{qs} - z_i) \tag{4.9}$$

$$w_{\text{eff}} = w_{qs}\Phi(0) + \sum_{i=1}^{N_{lag}} z_i \tag{4.10}$$

This indicial response function is used in the formulation of the state variable z, which describes the lagging effect on the downwash and is used in the computation of the effective angles α_{eff}, β_{eff}. These effective angles are used during the simulation for a look-up of the value of the attached lift coefficient $C_{\ell,\text{att}}$, which together with $C_{\ell,nc}$ forms the potential lift contribution. A low-pass filter is applied to this potential lift, which is used for the computation of an intermediate separation function, on which another low-pass filter is applied with a different time constant, to obtain the final expression for f which is used to interpolate between the attached and fully stalled lift to form the dynamic lift coefficient. The total lift coefficient is then obtained by addition of the non-circulatory component.

For a more detailed description and further ATEFlap model equations, please refer to the original work: [19] for the ATEFlap model, [14] for the underlying unsteady 2D potential flow description and [23] for the formulation of the Beddoes-Leishman type dynamic stall model.

4.2. Dynamic inflow model

The dynamic inflow model chosen is the Øye model, which in theory is modelled by two simple first order differential equations to capture the time lags which exist between the imposed load change and its effect on the induced velocity, one short-term effect directly following a change in velocity or pitch, the other a for wake-development following that. The equations used in the model are stated below:

$$y + \tau_1 \cdot \frac{dy}{dt} = k \cdot \tau_1 \cdot \frac{dx}{dt} \tag{4.11}$$

$$z + \tau_2 \cdot \frac{dy}{dt} = y \tag{4.12}$$

$$\tau_1 = \frac{1.1}{(1 - 1.3a)} \cdot \frac{R}{U} \tag{4.13}$$

$$\tau_2 = [0.39 - 0.26(\frac{r}{R})^2] \cdot \tau_1 \tag{4.14}$$

In these equations, r the local radius, R is the rotor radius, U the inflow velocity, a the axial induction, k a tuning parameter with default value 0.6 and the τ's are the time lag constants. The model is applied to the induced velocities, in these equations z is the final filtered velocity, y an intermediate value and x the quasi steady input (the induced velocity found in the BEM-iteration). Important, as also stated in [12], is to prevent the axial induction factor in equation (4.13) to exceed 0.5. For the solution of the equations, the algorithm given in [16] is used:

$$H = x_t + k \cdot \tau_1 \cdot \frac{x_t - x_{t-\Delta t}}{\Delta t} \tag{4.15}$$

$$y_t = H + (y_{t-\Delta t} - H) \exp(\frac{-\Delta t}{\tau_1}) \tag{4.16}$$

$$z_t = y_t + (z_{t-\Delta t} - y_t) \exp(\frac{-\Delta t}{\tau_2}) \tag{4.17}$$

Here backwards difference is used since in the time-marching simulation only data of previous time-steps is present. The model is defined for uniform inflow but in the implementation, for the use of turbulent inflow, the radial independence property of BEM is used to apply the model to each section individually and U in equation (4.13) is then the local axial inflow velocity without induction effects.

The implementation of the dynamic inflow model is done both in a Hansen-based solver as well as in a Ning-based solver. For the Hansen solver, after computing the axial induction factor, the corresponding dimensional induced velocities are corrected using the dynamic inflow model. A simple change in how flow angle is computed is effected (equation (2.2) is now computed using dimensional velocities rather than induction factors). For the Ning solver, for a given iteration value of ϕ, after computing the corresponding induction factors, the dynamic inflow correction is used to obtain dimensional velocity, which is then used in the slightly rewritten residual (equation (4.18)), where the induced velocities from the dynamic inflow model are used instead of the induction factors.

$$\mathcal{R}' = \frac{\sin(\phi)}{\cos(\phi)} - (V_n - V_{n_{ind}})/(V_t + V_{t_{ind}}) \tag{4.18}$$

4.3. Inflow simulation

For the inflow conditions used in the BEM solver, the NREL stochastic inflow turbulence code TurbSim is used, which is used to simulate atmospheric turbulence. This is needed for simulation of the turbulent inflow conditions of the DLCs. Among the methods that are implemented in the TurbSim software, two described by the IEC 64100-I standards are included [17][7]. These are the Kaimal and Von Karman models, for which a description follows. The fatigue analysis described in section 4.4 uses the inflow generated in TurbSim by these methods.

4.3.1. Kaimal Turbulence Model

The equation describing the Kaimal spectrum of the three wind velocity components in a Cartesian grid, is equation (4.19), as given in the the IEC61400-I standard, Ed. 3 [17].

$$S_K(f) = \frac{4\sigma_K^2 L_K/\bar{u}_{hub}}{\left(1 + 6fL_K/\bar{u}_{hub}\right)^{5/3}}, \quad \text{for} \quad K = u, v, w \tag{4.19}$$

$$L_u = 8.10\Lambda_U \qquad \Lambda_U = 0.7 * 60 \tag{4.20}$$

$$L_v = 2.7\Lambda_U \qquad \sigma_v = 0.8\sigma_u \tag{4.21}$$

$$L_w = 0.66\Lambda_U \qquad \sigma_w = 0.5\sigma_u \tag{4.22}$$

In the Kaimal turbulence model, neutral atmospheric stability is assumed.

4.3.2. Von Karman Turbulence Model

The equation describing the Von Karman spectrum of the three wind velocity components in a Cartesian grid, as given in [17], is equation (4.25). In this model, next to neutral atmospheric stability, isotropic turbulence is assumed.

$$S_u(f) = \frac{4\sigma_u^2 L/\bar{u}_{hub}}{\left(1 + 71(fL/\bar{u}_{hub})^2\right)^{5/3}} \tag{4.23}$$

$$S_{v,w}(f) = \frac{2\sigma_K^2 L/\bar{u}_{hub}}{\left(1 + 71(fL/\bar{u}_{hub})^2\right)^{11/6}}\left(1 + 189(fL/\bar{u}_{hub})^2\right) \tag{4.24}$$

$$L = \frac{7}{20}\Lambda_U \tag{4.25}$$

The standard deviation for each wind speed component are assumed to be equal.

4.4. Fatigue load calculation

The lifetime equivalent fatigue load is computed based on the description in the IEC 61400-1 Ed. 3 standard [17]. First, the time series data of the load in consideration is prepared for the rainflow counting by converting the data series to a collection of peaks and troughs. Then rainflow counting method is applied, which returns the cycle counts and the corresponding load range values.[1].

Subsequently, the load ranges (R_{eq}) per wind speed and the number of occurrences ($_i$) are binned to form a set of cycle counts per load range that is used to compute the equivalent load range the time series. This is the load range which at a frequency of 1 Hz would generate the same amount of fatigue damage in the time window of the simulation. For this, equation equation (4.26) is used to sum the contributions of the individual bins, where n_{eq} is 600 for a 10-minute time series and m=10 which corresponds to composite material.

$$R_{eq} = \left(\frac{\sum_i n_i R_i^m}{n_{eq}}\right)^{1/m} \tag{4.26}$$

For a single mean wind speed, every simulation is repeated six times using a different seed in TurbSim to obtain the generated flow field, and the resulting values for R_{eq} are averaged. At this stage, for a single mean wind speed, an equivalent load range is found for a 10-minute window. In order to generate the lifetime equivalent load spectrum, the analysis is repeated for every mean wind speed considered and the effect of these load cases added together and multiplied with the number of occurrences of the 10-minute window during its lifetime. The equivalent load that is computed as such is the result of [?].

[1]Rainflow counting script used: `https://gist.github.com/jennirinker/688a917ccb7a9c14e78f`, 2015 version. Webpage consulted on 11/06/2019.

$$L_{eq} = \left(\frac{\sum R_{eq}(U_i)^m n_{eq} p(U_i) n_T}{n_{eq,L}} \right)^{1/m} \tag{4.27}$$

In this equation, $n_{eq,L}$ is the number of 1 Hz oscillations in the lifetime of a turbine, $n_{eq} \cdot n_T$. The probability distribution used to compute the occurrence of the wind velocity corresponding to an individual bin, $p(U)$, is the Weibull distribution, as is customary for 10-minute wind averages. This two-parameter distribution is described by scale parameter A and shape parameter k, and the probability density function is given by equation (4.28)[?].

$$p_{Weibull}(U) = k \cdot \frac{x^{k-1}}{A^k} \cdot \mathrm{e}^{\left(-\left(\frac{U}{A}\right)^k\right)} \tag{4.28}$$

4.5. Optimisation method

In order to find the optimal actuation, the C++ BEM code is wrapped and used in a Python environment and used such that the BEM code can be ran as often as is required for the optimisation within a time-step for a given blade, without affecting the state variables of the previous time-step for the dynamic models. The optimisation algorithm for the pitch and the flap actuation is based on a full-knowledge of the system, and aimed at finding the optimal pitch and flap actuation to approach a set load output. The flapwise root bending moment is used for this and traced by using a moving average with a span of 10 seconds, which is aimed at reducing the high frequency oscillations with the actuation.

Using the constraints set on actuation speeds and bounds for the extreme values of the pitch and flap actuation, first an optimisation is run that attempts to attain the goal by pure flap actuation. The `minimize` function from the scipy optimize package is used to this end, with the Constrained Optimization BY Linear Approximation (COBYLA) setting. Should the optimisation fail to reach the desired load setting within the tolerance, which can happen due to the constraints on the actuation amplitude and speed, another optimisation is done. In this second optimisation, both the flap and pitch actuation is considered, where with a penalty on pitch actuation the flap actuation can be given a preference. Upon converging to a set of pitch and flap actuation, the loads are stored for this blade and this time-step. Next to the loads with the actuation present, the loads with null-actuation are stored for comparison in the post-processing. In each time-step, this computation is repeated for all individual blades, resulting in the desired data output. In the thesis work, the combined actuation functionality is not used, to limit the captured effect to that induced by the flap actuation only.

4.6. Verification

For the verification of the implementation of the aerodynamic model ATEFlap, the results, using a NACA64-418 aerofoil are compared to the original results of the paper in [19], which should match precisely. The results are generated for different reduced frequencies, for a change in angle of attack and flap deflection. For the implementation, first a BEM code with the solver method as described in Hansen is implemented in Python, for which a first comparison of the output versus the paper is done. Then, the same code is implemented in the in-house C++ BEM software, which uses the Ning-type solving technique. Again, the test cases from the original paper [19] are produced for verification. The results from the latter implementation can be found in chapter 5. A similar process is followed for the implementation of the Øye dynamic inflow model, where the comparison is done with validation data.

4.7. Validation

For the validation of the implementation of the ATEFlap aerodynamic model, the data from the AVATAR project (section 2.2.3) is used. First, the steady data from the project is pre-processed using the Pre-processor for ATEFlap Dynamic Stall Model, ver. 2.05. This takes the steady lift, drag and moment coefficients for different steady flap angles as input and following the method in (section 4.1.1, [19]) provides the `.ds` data which is used as an input in the C++ BEM code and contains the $C_{l,st}$, $C_{l,att}$, $C_{l,fs}$ which are needed for the computation of $C_{l,dyn}$. Using this setup, the unsteady cases from the AVATAR experiment are run with the ATEFlap aerodynamic model, to compare the behaviour for oscillation of

the flap in attached flow, partial stall and full stall conditions. By comparing the modelled output with the experimental data, a qualitative and quantitative evaluation of the model is done.

Since the wind-tunnel data for drag only concerns the pressure drag, and the main concern for the model is the lift coefficient, this is the parameter that is validated for the model. In order to have a measure for how well the data fits in the attached and fully stalled conditions, where the lift coefficient forms hysteresis loops in the shape of a Lissajous oval, a parameterisation of the hysteresis loops is done by using the parametric equations 4.29 and 4.30.

$$\begin{cases} \beta = A_\beta \sin(\omega t + \phi_1) & (4.29) \\ C_l = A_{C_l} \sin(\omega t + \phi_2) & (4.30) \end{cases}$$

For application on the AVATAR data, some of these parameters can be parameterisation, the angular frequency ω can be obtained from the reduced frequency at which the flap actuation was performed (k), the flow speed and semi-chord length. The amplitude A_β is equal to half the difference between the minimum and maximum flap angle in radians. As the first phase offset is set to zero for the model simulation, the fit of parameters for the simulation can be obtained from fitting a least-squares to the lift coefficient obtained from the ATEFlap model and the corresponding time vector using the second parametric equation. The phase offset in equation (4.30) is negative for a counter-clockwise loop, and positive for a clockwise hysteresis loop.

For the AVATAR data, a time vector corresponding to the sampling frequency of 300 Hz and the length of the data is used and a least-squares fit for both parametric equations is done, and the phase offset ϕ_1 is subtracted from ϕ_2 to be consistent with the zero phase shift used for the model simulation. In this manner, a quantitative comparison of both Lissajous curves can be performed and the performance of the model assessed.

5

Verification and Validation

This chapter deals with the verification and validation of the ATEFlap model that was implemented. As the model is a two-dimensional unsteady aerofoil aerodynamics model, the verification and validation are done for a single blade section. For the dynamic inflow model, a validation of simulated rotor shaft torque against measurement data is done for a prescribed pitching motion.

5.1. Verification of the ATEFlap implementation

Since the model description in [19] is closely followed in implementing the aerodynamic model, the presented plots in that original work have been reproduced as a verification procedure. This has been done for figures 3.1 and 3.2 in section 5.1.1 and figures 4.4 to 4.10 in section 5.1.3.

5.1.1. Step change in angle of attack

As the aerodynamic model is capable of capturing the wake-memory effect, this is demonstrated by simulation of two step changes of angle of attack. The first is in the attached region and therefore leads to an increase in lift, which under steady assumption would occur instantly, though physically this circulatory lift exhibits a lag, which is described by the Wagner function, for which the truncated indicial response function used in the model is an approximation. The lift over time as can be seen in figure 5.1, shows how the model captures this lag effect. It should be noted that, if the non-circulatory terms are included and a Heaviside step function is used as the input, this gives rise to a non-physical peak in the lift coefficient. Using a logistic function instead, such as the Sigmoid function, to approximate the Heaviside input, gives a smooth, realistic response.

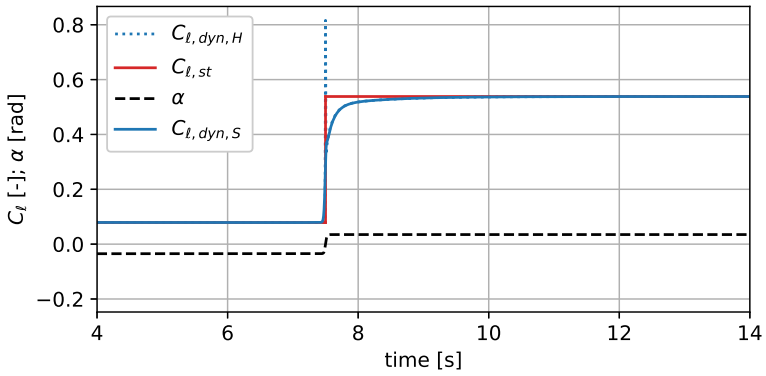

Figure 5.1: Heaviside change in angle of attack from -2 to 2 degrees, which shows the circulatory lift development plus non-physical peak, and similar jump, using a sigmoid function, showing smooth behaviour.

In figure 5.2 the effect over time of the dynamic stall followed after a surge in lift due to the faster

acting potential flow effect can be observed, which illustrates that the timescale at which potential flow phenomena occur is smaller than that of stall, an important consideration for fast flap actuation systems.

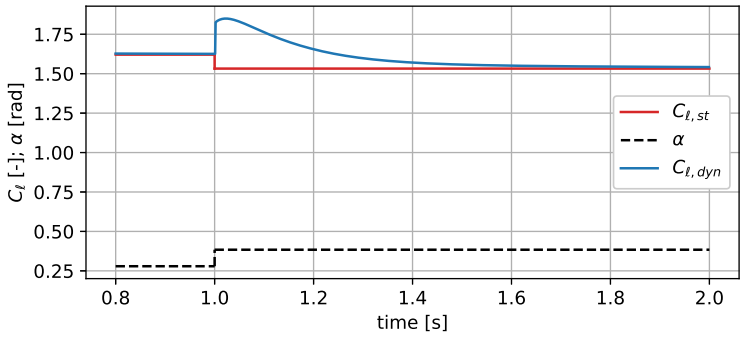

Figure 5.2: This figure shows the ATEFlap model response to a step in angle of attack from 16 to 22 degrees, showing the model response upon entering stall.

These figures (figure 5.1 and figure 5.2), though created with different aerofoil data and timescales, qualitatively follow the behaviour shown in the original work of Bergami and Gaunaa.

5.1.2. Steady lift behaviour

In figure 5.3 the steady data that was used in the ATEFlap model is shown. The vertical black dashed lines indicate where the verification of the model is performed.

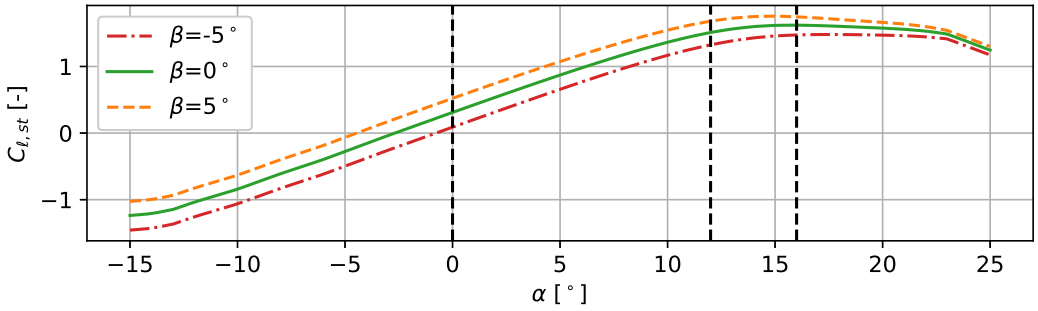

Figure 5.3: The steady lift curves for the NACA 64-418 aerofoil with flap, at β equal to -5, 0 and 5 degrees.

5.1.3. Hysteresis effects in oscillatory motion

The dynamic effects (circulatory, non-circulatory and stall) result in the case of a harmonic oscillatory excitation in either pitch or flap angle in a hysteresis effect in the aerodynamic loads. The coefficients of lift, drag and moment found by use of the model for a NACA 64-418 aerofoil are shown for different reduced frequencies $k = \frac{\omega \cdot V_{rel}}{c/2}$. Here V_{rel} is the relative inflow velocity as seen by the aerofoil, ω the oscillation frequency and $c/2$ the semi-chord length. For a reduced frequency of 0.1, the hysteresis plots in this section have been generated. The behaviour for zero flap angle and oscillating angle of attack (for this simulation the angle of attack is set equal to pitch, effectively disabling the BEM solver) is shown in section 5.1.3. The angle of attack is varied with a unity amplitude, with a mean of 0, 16 and 22 degrees for the different figures, respectively. A similar simulation was performed for the flap angle variation, which led to similar hysteresis effects for C_l and C_d, but the effect on C_m remains linear for a reduced frequency of 0.1. Only for the high reduced frequency of k=0.5, the reference data from [19] shows hysteresis in the C_m curve. This is the only instance in which the results of the current implementation deviate visibly from the reference data, though the difference is rather small (maximally about 0.004).

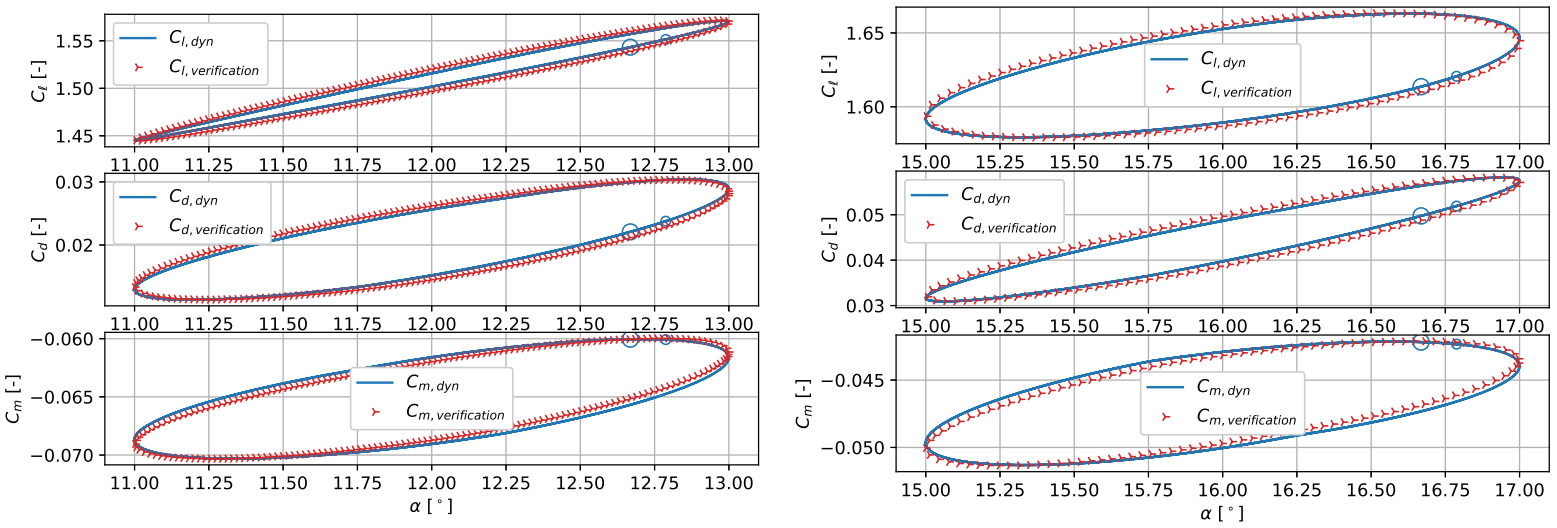

Figure 5.4: The lift, drag and moment response for a harmonic oscillation of the angle of attack with a mean of 12° (left) and 16° (right), reduced frequency of 0.1 and 0° constant flap angle.

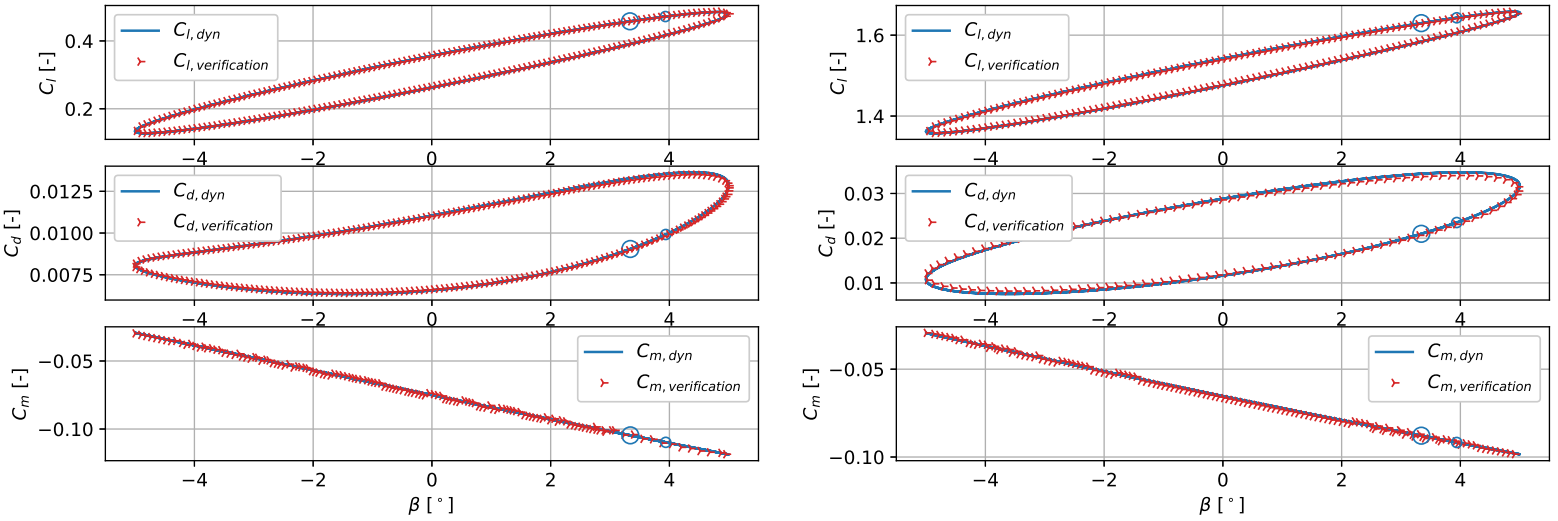

Figure 5.5: The lift, drag and moment response for a harmonic oscillation of the flap, with a mean of 0°, reduced frequency of 0.1 and amplitude of 5°. The angle of attack is constant at 0° (left) and 12° (right).

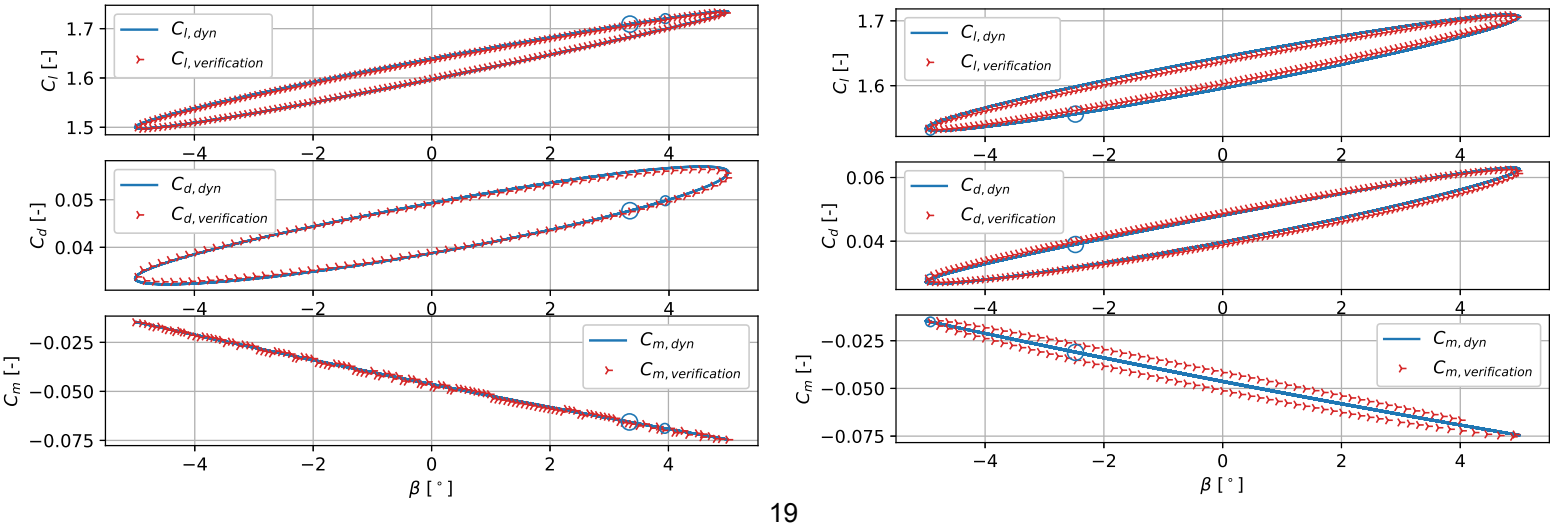

Figure 5.6: The lift, drag and moment response for a harmonic oscillation of the flap, with a mean of 0°, amplitude of 5°, reduced frequency of 0.1 (left) and 0.5 (right). The angle of attack is constant at 12° (left) and 16° (right).

5.2. Validation of the aerodynamic model

For the validation of the implementation of the ATEFlap model, the wind tunnel measurement data from the AVATAR project, work package 3, task 3.1 is used [10], as outlined in section 4.7. The DU 95-W-180 aerofoil, equipped with a rigid (not cusped) trailing-edge flap extending 20% in chordwise direction (total chordwise length 0.6 m), has been used in the AVATAR project to experimentally obtain the dynamic behaviour of an oscillating rigid flap at different reduced frequencies and mean angles of attack. The experiments are done for both free and forced transition, here the data from the free transition setup is used. In figure 5.7, the steady data that has been used as an input to the preprocessor is shown, as well as the angles of attack at which the unsteady cases are performed.

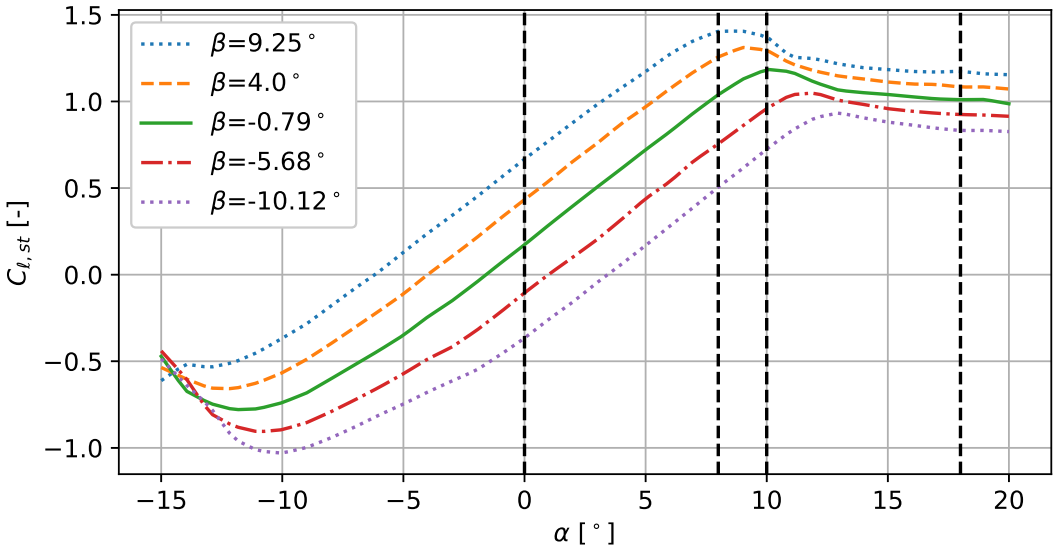

Figure 5.7: The experimental steady data for different flap deflections. The vertical dashed lines indicate where the angles of attack lie at which the unsteady cases are located.

For the experimental data, displayed in orange, one standard deviation is shown as a lighter shaded area around the mean values. In dashed lines (experimental) or dash-dot lines (model) the Lissajous figure fit is shown, for which the characteristic parameters are given in the lower-left legend. In order to indicate the direction of the loops, a small circular marker followed by a large one is shown for both the experimental data as well as the model output. In this section, results are shown for the lift coefficient in low and high reduced frequency flap oscillation, at mean angles of attack of 0°, 8° and 16°, corresponding to cases UNST1, 11, 13, 23, 28, 29 of the AVATAR experiment. The comparison data (plots and a table containing the parameters of the Lissajous fits) for the other cases can be found in chapter A.

In the plot on the left in figure 5.8, the model behaviour is compared against measurement data for the case named UNST1, which corresponds to attached flow (with α=0) and oscillation at a low reduced frequency of 0.01. At these conditions, the model output fits the data well, with only a small offset in the phase shift and amplitude found.

At a high reduced frequency, such as on the right in figure 5.8, the hysteresis effect in the C_l loop is increased. The experimental data displays a slightly larger hysteresis effect, which results in a larger offset in phase. Since the average slope of the model data is lower than that of the experimental data, the corresponding amplitude is also slightly lower. As the flow is completely within the attached flow regime in these plots, the lift coefficient behaves in a linear manner (the steady lift forms a straight line whereas the unsteady results are perfect ellipses).

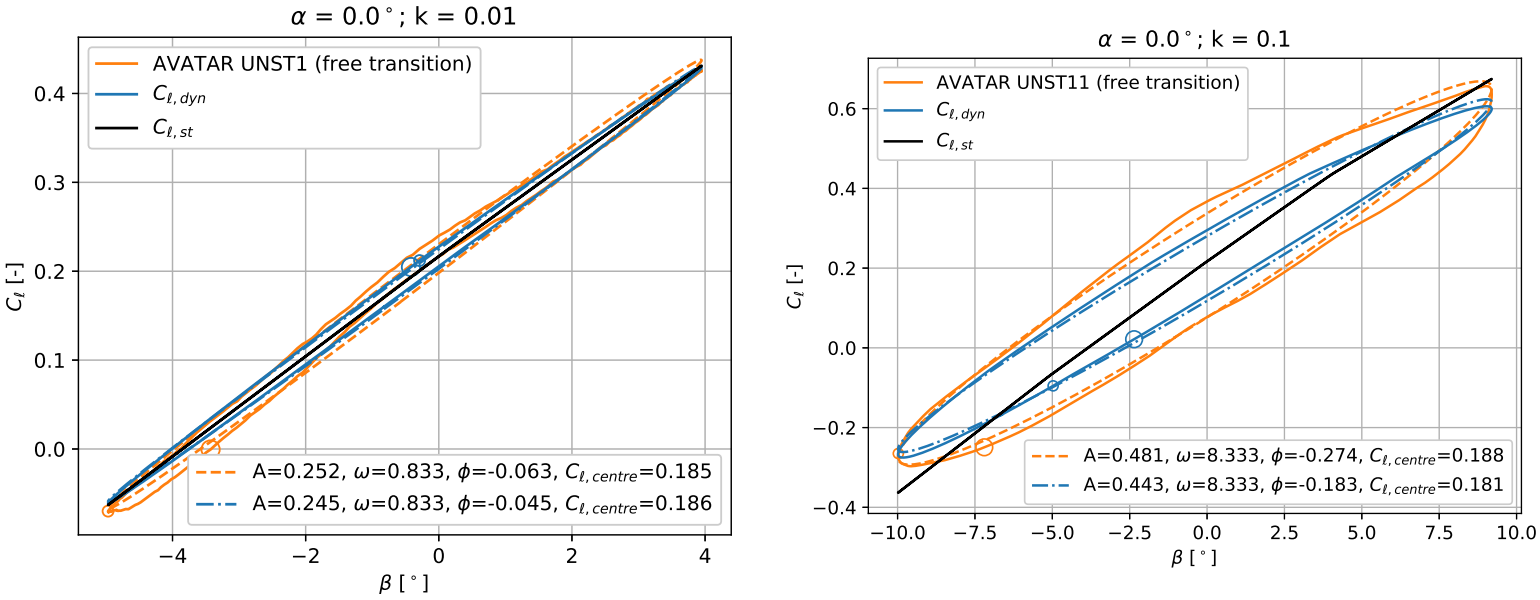

Figure 5.8: Hysteresis behaviour for a low (left) and high (right) reduced frequency oscillation, varying flap angle at zero angle of attack.

In figure 5.9, since the mean angle of attack is 8° here, the steady data starts showing a slight deflection, indicating that the nonlinear lift region is entered. The model behaves well compared to the measurement data, even the shape deflection toward the higher flap angles is captured (the deviation of the test data from the ellipse shows that here the linear lift region is exited). There remains an offset in phase though, visible in the width of the elliptical shape.

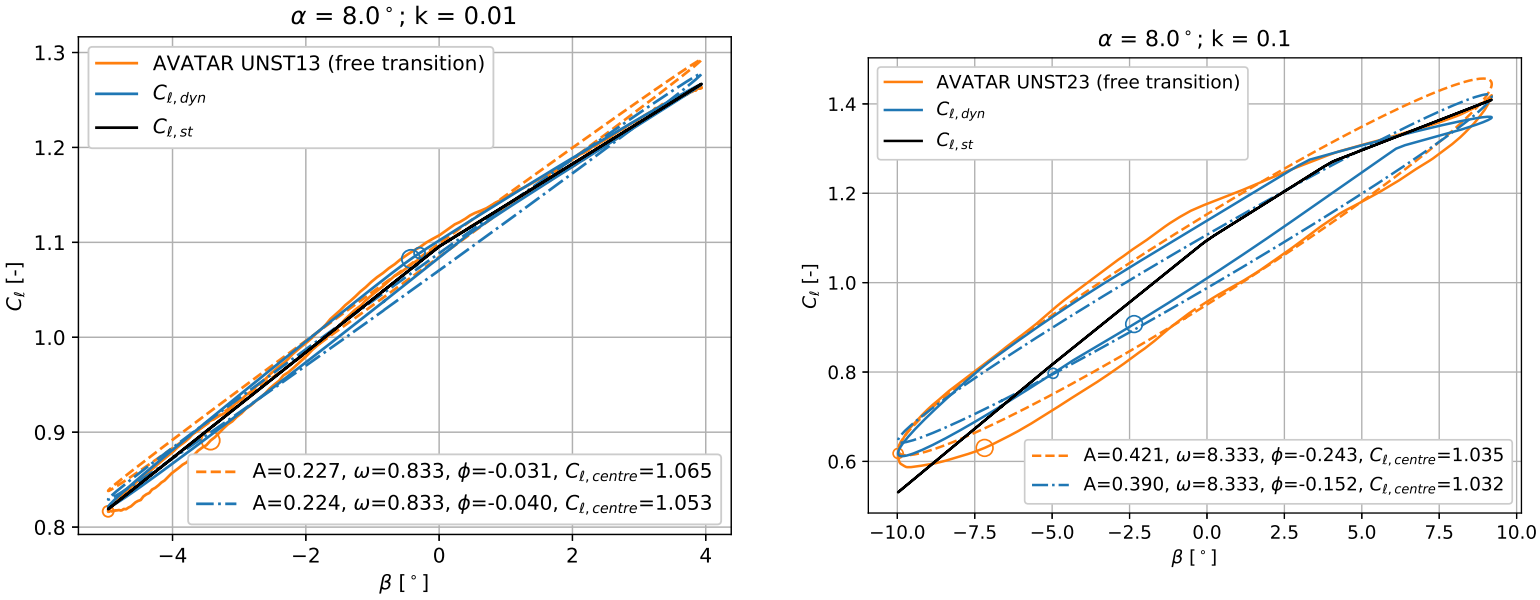

Figure 5.9: Hysteresis behaviour for a low (left) and high (right) reduced frequency oscillation, varying flap angle at zero angle of attack.

In figure 5.10, the hysteresis behaviour is shown for large flap actuation (between -10° and 10°) at a constant angle of attack of 10 °. At this angle of attack, the $C_{l,max}$ is reached and even surpassed for $\beta = 10°$. This results in the large spread in data (high standard deviation) between 5° and 10°. However,

interestingly enough this happens only at the low reduced frequency, the high reduced frequency displays behaviour that is more consistent, and can be described as dynamic stall.

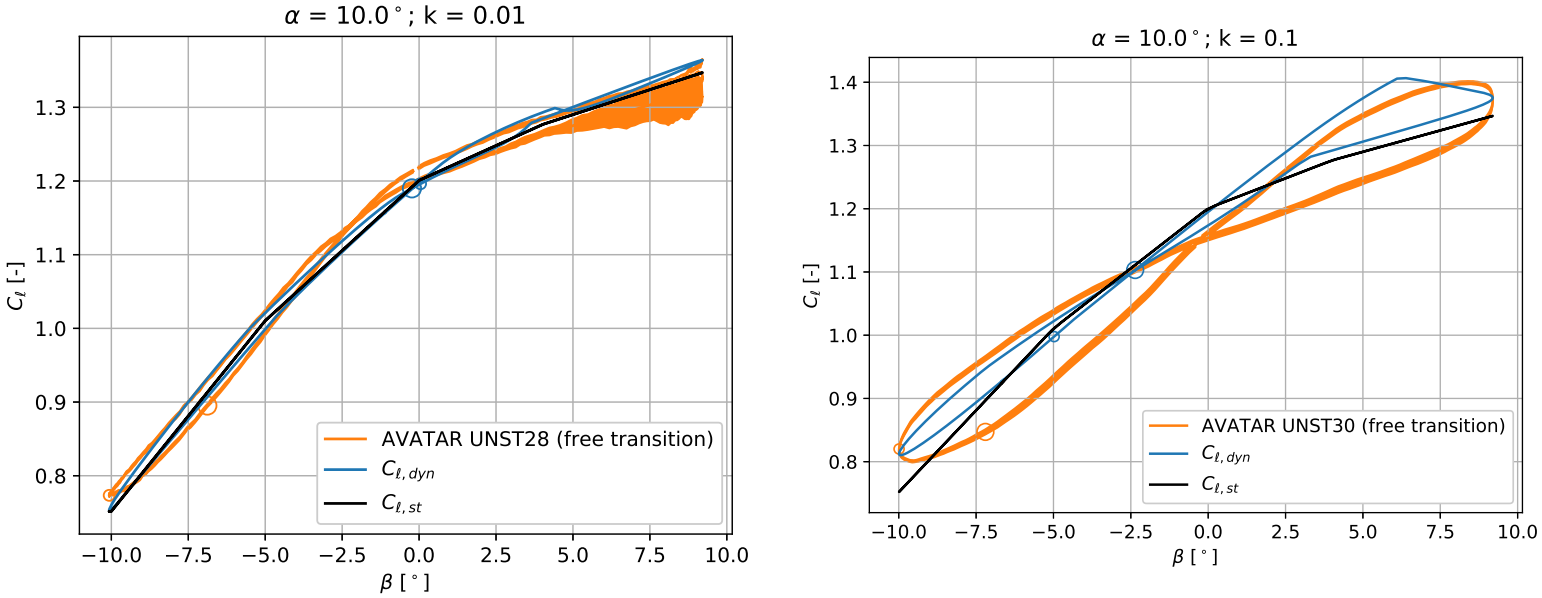

Figure 5.10: Hysteresis behaviour for a low (left) and high (right) reduced frequency oscillation, varying flap angle at ten degrees angle of attack. Displays partial stall behaviour.

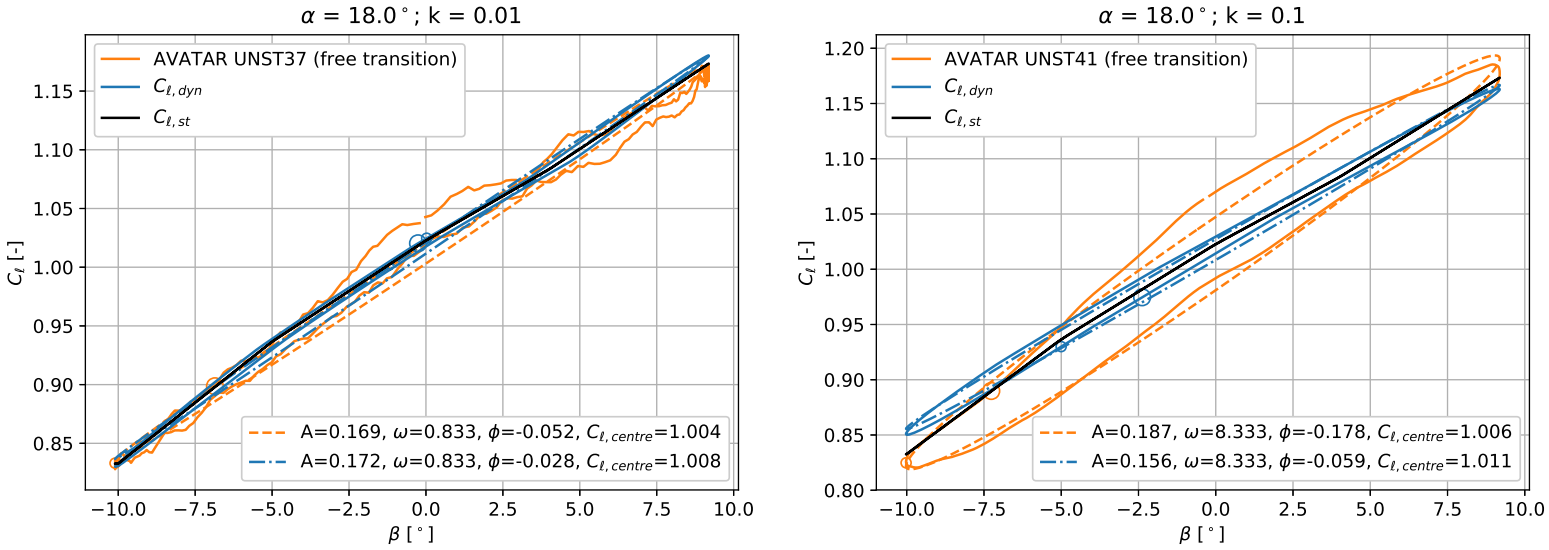

Figure 5.11: Hysteresis behaviour for a low (left) and higher (right) reduced frequency oscillation, varying flap angle at eighteen degrees angle of attack. Displays deep stall behaviour.

5.3. Validation of the dynamic inflow model

The implemented Øye dynamic inflow model is validated by comparing the simulated rotor shaft torque by the model to experimental data provided in figure 9.7 of [16]. The Tjaereborg 2 MW wind turbine is simulated during sixty seconds, with initially zero pitch. After two seconds, pitching is started at a constant speed to a value of 3.7 degrees, which is attained after one second. After 32 seconds, the pitch is changed back, similarly during one second. In order to obtain the agreement shown in figure 5.12, the dynamic inflow model parameter k_{di} as well as the transition value of the axial induction to enter the empirical Glauert-corrected region (a_c) are tuned to $k_{di} = 0.77$ and $a_c = 0.225$. The value for the transition induction value lies in the suggested region of 0.2-0.4 by [16], the default value for the dynamic inflow model parameter is 0.6. It must be noted that the cutoff a_c is different when using the Ning approach for the

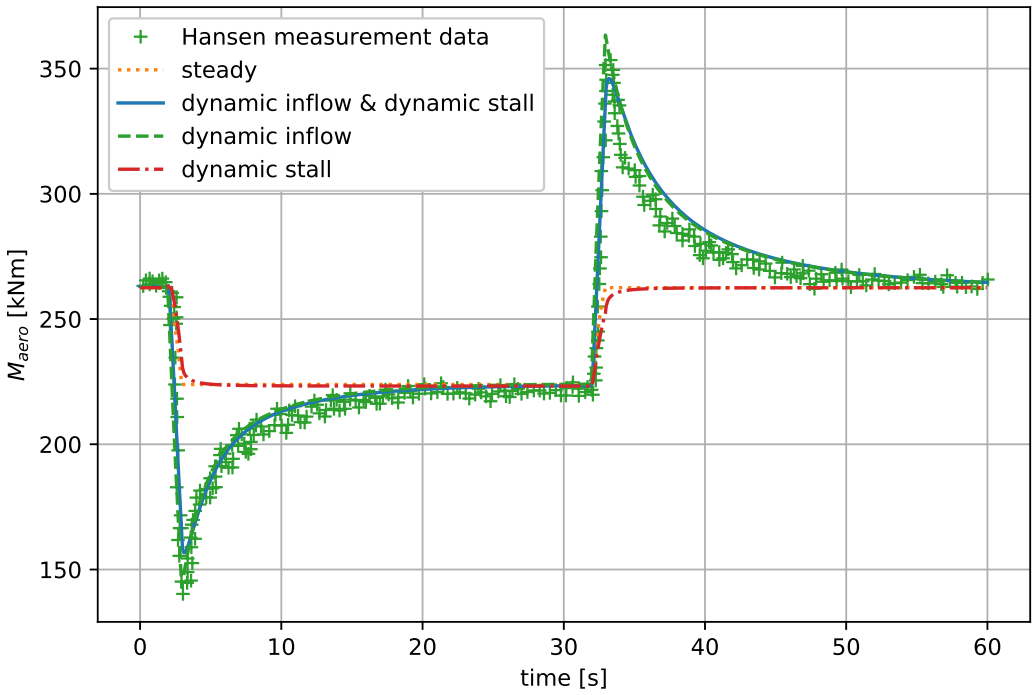

Figure 5.12: Dynamic response of the modelled shaft torque of the Tjaereborg 2 MW wind turbine for pitching motion, with and without dynamic inflow model. Pitching motion: for t<2s and t>33 seconds, pitch is zero, between 3 and 32 seconds the pitch equals 3.7 degrees). Used dynamic models: ATEFlap aerodynamic model (dynamic stall), ye dynamic inflow.

In the dynamic response, the overshoot resulting from the dynamic wake is captured and agrees well with the measurement data. When additionally enabling the ATEFlap aerodynamic model, the peaks in the response get rounded due to the time-lag effect of the potential flow component of the ATEFlap model, otherwise the response remains the same. By observing the response with only the dynamic stall model enabled, the need for the additional dynamic inflow model becomes apparent.

6

Turbine-scale effects

The results in this section are obtained by simulating a Tjaereborg blade with a NACA 64-418 ATEF-equipped aerofoil. Effects regarding the flap placement, actuation speed and loads are discussed, as well as the effect of the dynamic models on the results.

6.1. Effect of dynamic models on loads

In this section, the effect of the dynamic models (ATEFlap aerodynamic model and the Øye dynamic inflow model) are investigated. Two Heaviside step functions (in freestream velocity, flap actuation and pitch actuation), as well as the response to low and high reduced frequency oscillation of the pitch/flap actuation. The results are shown for the flapwise root bending moment $M_{flapwise}$ and the aerodynamic moment M_{aero}.

In section 6.1, the behaviour described before in section 5.1.1, is seen on a turbine scale to affect the simulation in a similar manner. However, a similar actuation, though with a different flap configuration, is displayed in section 6.1, which due to the absence of a non-physical actuation results in a smooth response without non-physical peaks.

6.2. Spanwise ATEF placement and actuation speed

In order to study the effect of the spanwise flap placement, the blade definition has to be altered. This has been implemented such that a percentage range can be given between which the flap placement is applied. An issue that could occur is when the blade definition is done for a relatively small amount of radial sections, where on the borders of the flap range the interpolation between flap and non-flap section loads would be incorrect. In order to prevent this, two additional sections are added, of the flap aerofoil type, close to each other, on the borders of the flap range. These contiguous sections are

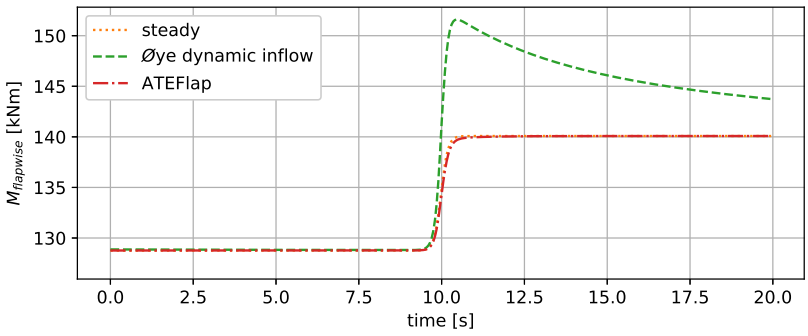

Figure 6.1: Response in time of $M_{flapwise}$ due to a sigmoid variation in flap angle, from 0 to 10 °, at a flap distribution from 70 to 90% of the blade, with the DU95W180 aerofoil from in the AVATAR validation.

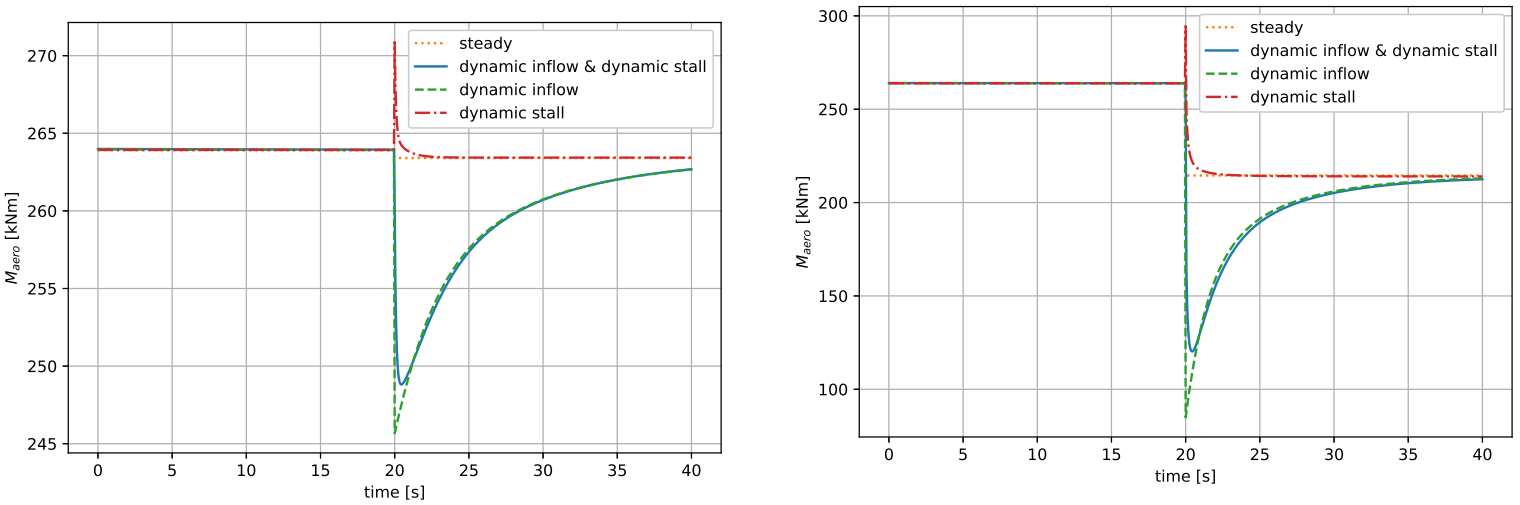

Figure 6.2: Tjaereborg responses to a Heaviside step in actuation, left: flap actuation, 0° to 5°, right: pitch actuation, 0° to 5°.

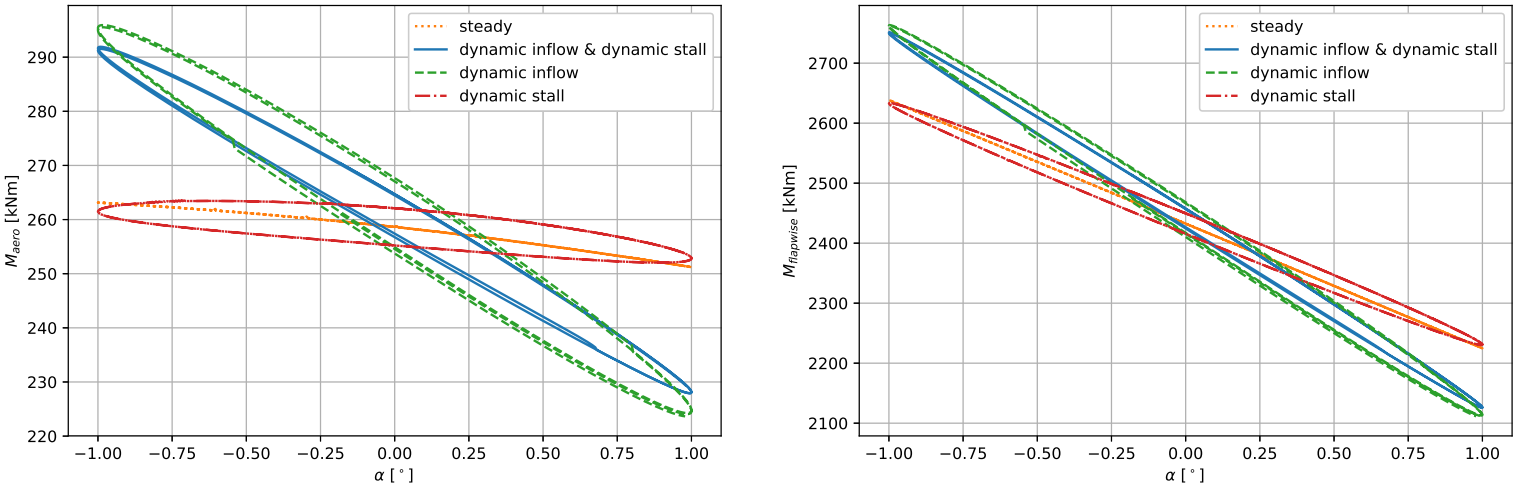

Figure 6.3: Tjaereborg hysteresis loops for M_{aero} and $M_{flapwise}$ from a harmonic pitch oscillation. Inflow speed 8.7 m/s, reduced frequency of 0.05, oscillation amplitude of one degree.

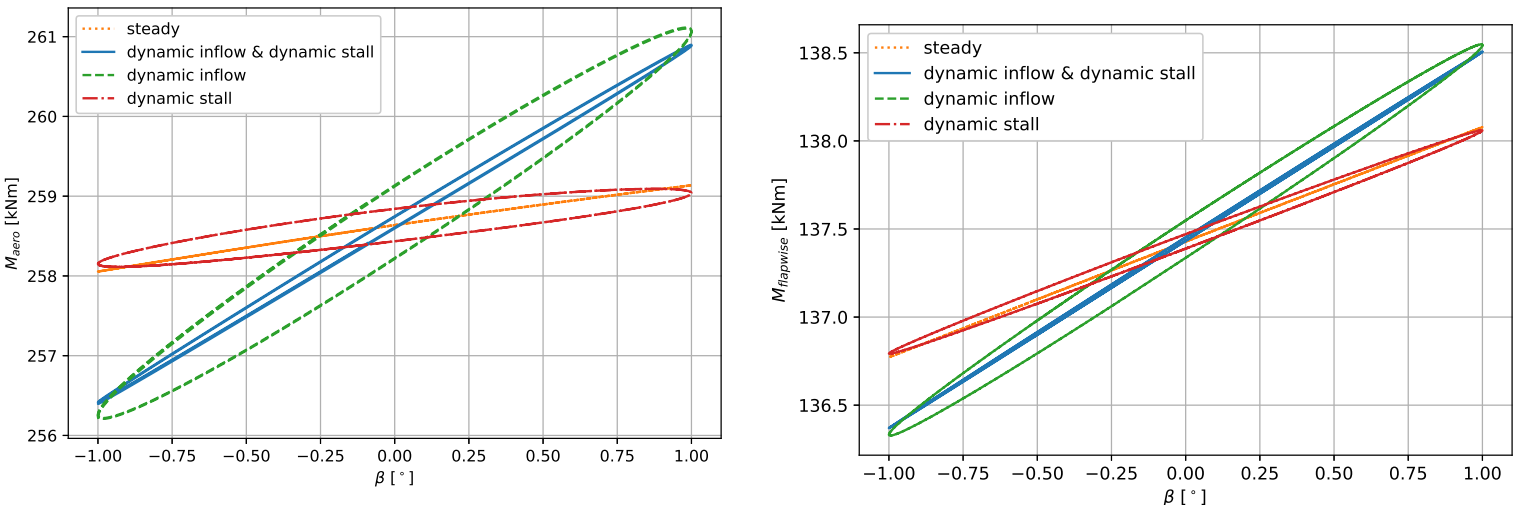

Figure 6.4: Tjaereborg hysteresis loops in M_{aero} and $M_{flapwise}$ from a harmonic flap oscillation. Inflow speed 8.7 m/s, reduced frequency of 0.05, oscillation amplitude of one degree.

identical, except for the activation of flap actuation, which is disabled for the section on the flapless side. The interpolation of the loads in the post-processing will therefore only happen on the small gap between these sections, which is set to one centimetre.

In figure 6.5, the effect of the spanwise extension of flap sections, as compared to the same configuration without flap actuation is shown. Since the original polars are swapped for the flap polars in the desired region, the comparison is always performed using the same blade layout in terms of polars, with the comparison being between actuation enabled and disabled. In the figure, for each spanwise extension, the middle dot indicates the load without flap actuation, the dot above and below this the steady values for a constant flap actuation at -5 and 5 degrees. Lastly, the triangular markers indicate the minimum and maximum values that are obtained when the flap is oscillated at a high reduced frequency (locally with a value for k of about 0.25, with ω= 20°/s). This is to indicate the upper and lower limits that arise from the dynamic response in load output.

The potential of the use of active flow control using ATEF is highly affected by the dynamic effects modelled by the ATEFlap- and dynamic inflow model, as became clear from section 6.1. In this subsection it is considered how the load changing potential of ATEF is affected by the actuation speed. The results show a remarkable feature, that is, even though the steady difference between the two is identical, the actuation speed has a very large effect on the loads experienced. This is due to the dynamic inflow model, intended to capture the wake-dynamic effects such as seen in figure 5.12.

In section 6.2, it is therefore observed that the difference between the steady and dynamic values is larger than that for a lower speed actuation, see section 6.2. This significant effect emphasises that the actuation and induced load fluctuation can induce an additional potential compared to the values indicated by the steady values.

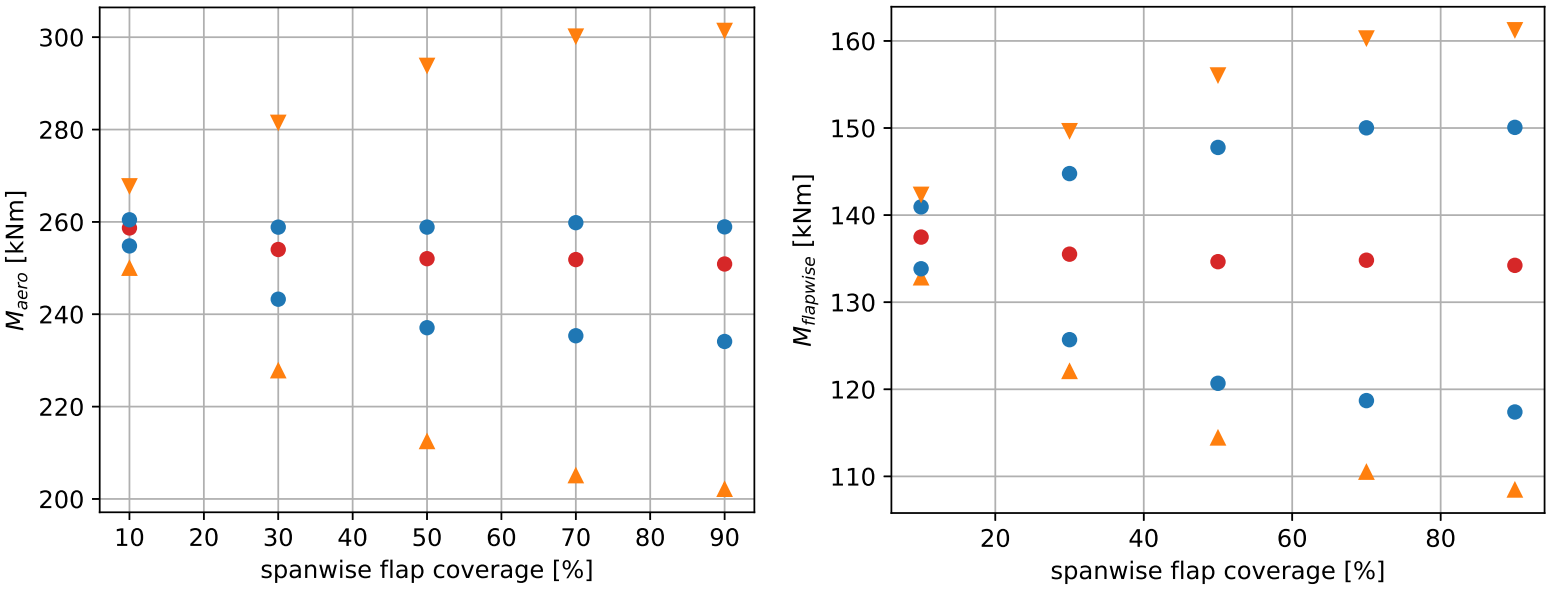

Figure 6.5: Steady load-changing potential of NACA 64-418 profile equipped with a trailing edge flap (covering 10% of the chord). Max amplitude of the flap actuation is 5°. The red dots indicate the behaviour without flap actuation, the blue dots the static deflection values. The orange triangular markers show the maximal effect of active actuation, with an actuation speed of 20° per second.

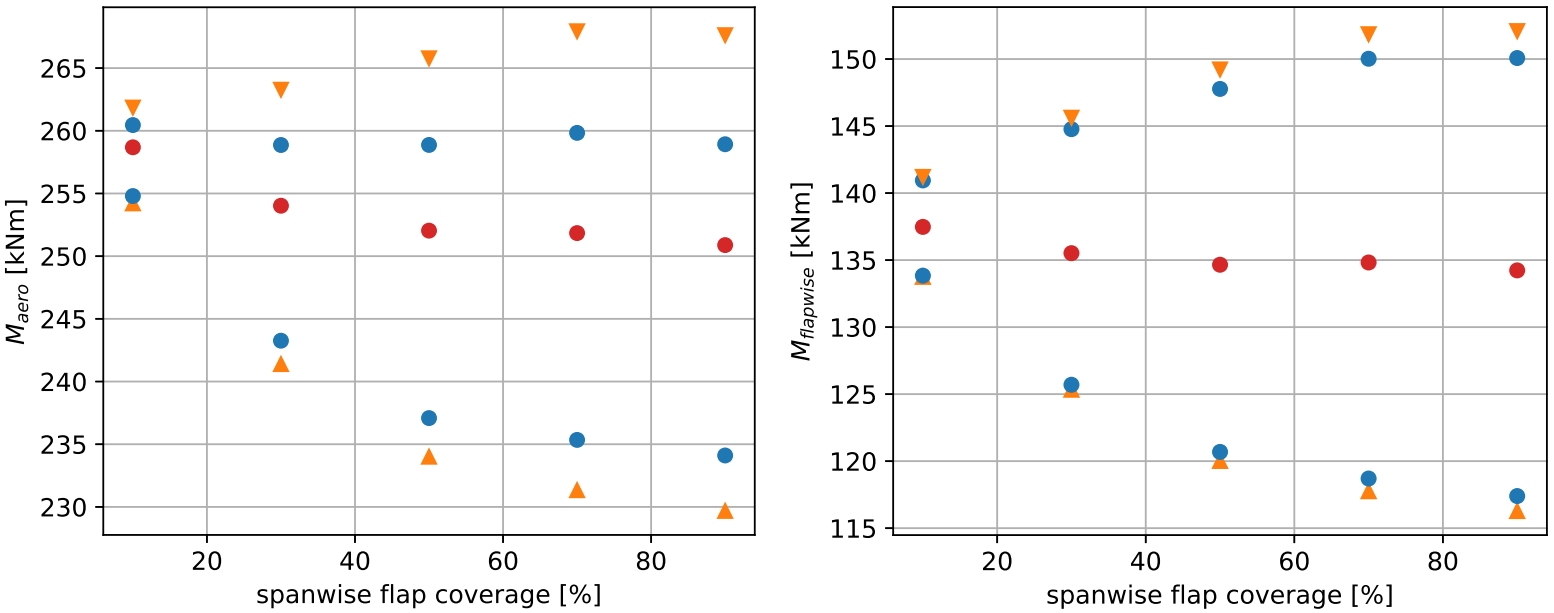

Figure 6.6: Similar to figure 6.5, this instance with an actuation speed of 5° per second.

6.3. Fatigue

In this section, the fatigue analysis as described in section 4.4 is performed on the Tjaereborg wind turbine, equipped with a flap section between 70 and 90% of the span. Additionally some plots relating to the DTU 10 MW reference wind turbine are shown.

A 10-minute simulation is done for three seeds at wind speeds from 5 to 25 m/s, with solely flap actuation (maximally 20 degrees, actuation speed of 20°/s), at zero pitch, with the dynamic inflow model disabled. The flapwise root bending moment is then rainflow-counted resulting in results for each seed and wind speed in the form of figure 6.7. Using these results, the graph in figure 6.8 has been created, which shows the benefit of using flaps for the fatigue loads. The average lifetime equivalent root flapwise bending moment for the Tjaereborg wind turbine under these simulation conditions is 35.5 kNm with flap actuation, versus 43.3 kNm without.

In section 6.3, a the time-wise load output from the optimisation is shown for the DTU 10 MW wind turbine, for which in the configuration, the flap design is not sufficient to properly alleviate the loads, causing the flap to constantly operate at the maximum deflection value (here 5°). From this plot it can be observed that the effect on $M_{flapwise}$ is larger than that on M_{aero}.

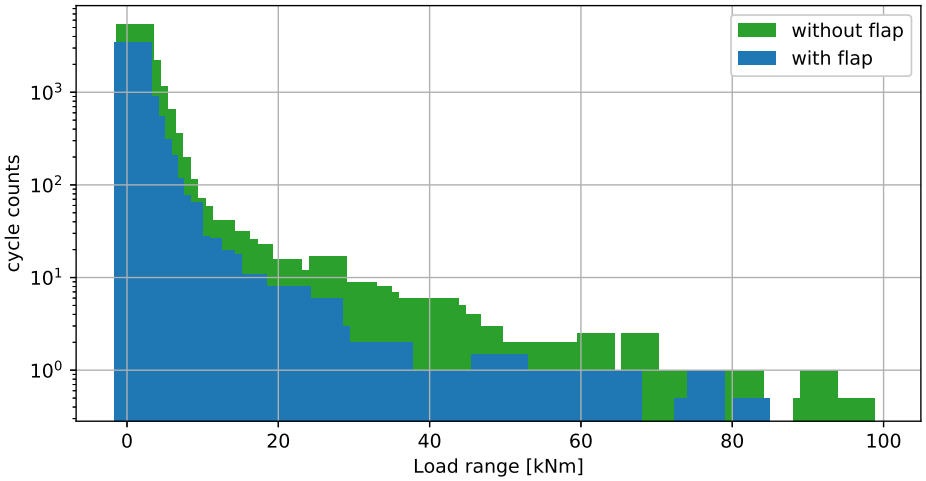

Figure 6.7: Rainflow-counted flapwise root bending moment for the Tjaereborg wind turbine at mean inflow speed of 11 m/s, flap angle up to 20 degrees and flap speed of 20°/s.

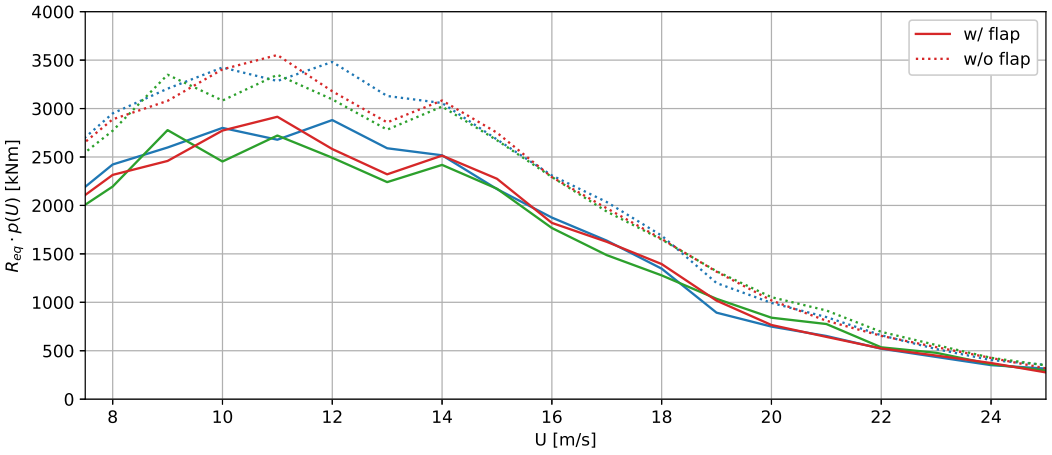

Figure 6.8: Rainflow-counted flapwise root bending moment for the Tjaereborg wind turbine from 7.5 m/s to 25 m/s, data for three different turbulence seeds shown.

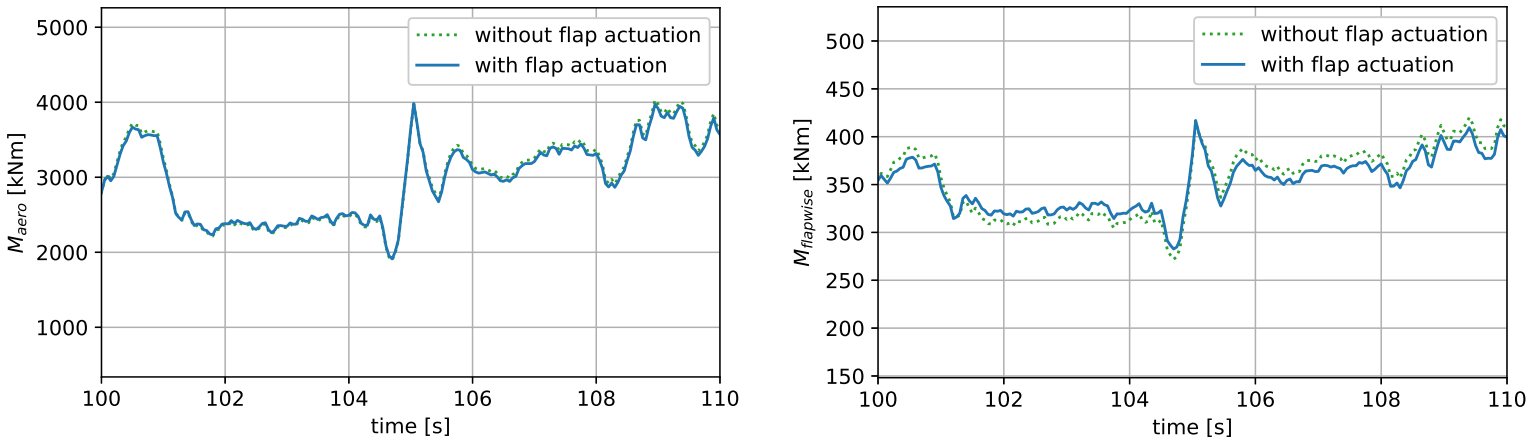

Figure 6.9: Time-wise load response for the DTU 10 MW reference wind turbine during a 10 second time window.

In figure 6.10, for a single seed with normal atmospheric turbulence (Von Karman), mean inflow velocity of 10 m/s, three scaled versions of the DTU 10MW reference wind turbine are evaluated with and without flap actuation. The flap covers the span from 70% to 95% and has a maximum actuation speed of 20°/s, maximum flap deflection of 5° with a flap-equipped NACA 64-418 section. time discretisation of dt=0.05 seconds. From this plot, no direct conclusions can be drawn as the data presented is limited, though an indication that the reduction of the equivalent fatigue load for the root flapwise bending moment is equivalent in this case to an upscaling by 2 percent can be observed.

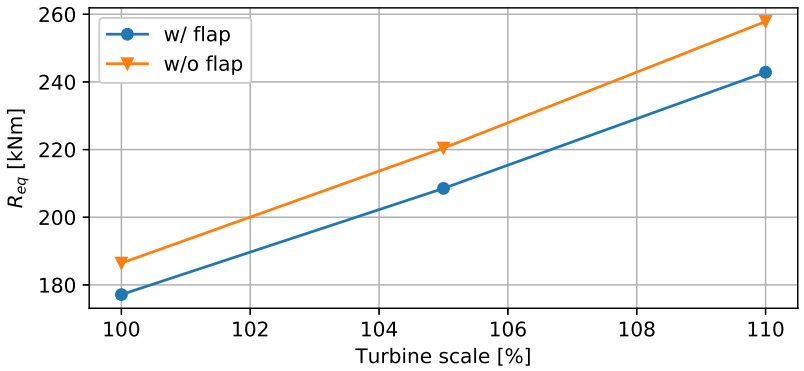

Figure 6.10: Equivalent fatigue load for the root flapwise bending moment at 10 m/s, for the DTU 10 MW reference wind turbine, equipped with a flap from 70% to 95% span and two linearly upscaled versions.

7

Conclusions and Recommendations

In modelling Adaptive Trailing Edge flaps, the use of dynamic models is of high importance, and the effect on the dynamic loads is significant and cannot be neglected. For any actuation, whether it be pitch or flap actuation, the effect of the dynamic wake captured by the Øye dynamic inflow model is largest, about 10% of the flapwise and aerodynamic moment for an actuation reduced frequency of 0.05.

The validation study showed that the ATEFlap model is well-capable of predicting the lift coefficient in different flow regimes, performing best for low-reduced frequency, attached flow, though still able to capture the flow phenomena in near-stall and deep stall, for the latter only at low reduced frequencies. Important for a good functioning of the model is correct preprocessing and constraining the actuation, as nonphysical jumps in input will result in nonphysical output from the non-circulatory part of the ATEFlap formulation, that may impair the simulation success.

When used simultaneously, the ATEFlap model has a smoothing effect upon the response of the Øye dynamic inflow model, as the effect is opposing the overshoot in loads given by the dynamic inflow model. As both models capture different dynamic effects, the use of both is advisable. Furthermore, the effect captured by the dynamic inflow model suggests that, not only the effect that can be realised by the steady difference between the lift polar of a section with and without flap actuation matters. The dynamic effects can amplify these load variations and this could provide an additional dynamic load variation compared to that anticipated from the steady data.

An important recommendation is to include elastic effects, which due to time constraints did not make it into the scope of the thesis. For a wind turbine blade, which generally exhibits a significant flapwise and torsional flexibility, a flap system can only be designed properly if these effects are taken into consideration, and used in the design process to make optimal use of the coupling between aerodynamic and structural effects. The thesis work treated the aerodynamic aspect of the system, though it must be stressed that for realistic simulations, aero-elasticity must be considered.

Bibliography

[1] A.E. Abott I.H., von Doenhoff. Theory of Wing Sections. Dover Publications, 1959.

[2] T. K. Barlas and G. A.M. van Kuik. Review of state of the art in smart rotor control research for wind turbines. Progress in Aerospace Sciences, 46, 2010.

[3] T.S. Beddoes. Vertica, 8(1):55–71.

[4] L. Bergami. Adaptive Trailing Edge Flaps for Active Load Alleviation in a Smart Rotor configuration, DTU Vindenergi Report 2013. Number March. 2013.

[5] L. Bergami. Smart Rotor Modeling, Aero-Servo-Elastic Modeling of a Smart Rotor with Adaptive Trailing Edge Flaps. Springer, 2014. ISBN 9783319073644.

[6] L.O. Bernhammer. Smart Wind Turbine: Analysis and Autonomous Flap. PhD thesis, Delft University of Technology, 2015.

[7] L. Kilcher B.J. Jonkman. TurbSim User's Guide Version 1.06.00. 2012.

[8] Croce A. et al. Bottasso, C.L. Load mitigation for wind turbines by a passive aeroelastic device. Journal of Wind Engineering and Industrial Aerodynamics, 2015.

[9] P. Bæk. Unsteady Flow Modeling and Experimental Verification of Active Flow Control Concepts for Wind Turbine Blades. 2011.

[10] Daniel Baldacchino et al. C.J. Simao Ferreira. Unsteady measurements of the DU95W180 airfoil with oscillating flap. 2015.

[11] Thomas Buhl et al. Damien Castaignet, Thanasis Barlas. Full-scale test of trailing edge flaps on a vestas v27 wind turbine: active load reduction and system identification. 2012.

[12] Peters D.A. Gaonkar, G.H. Review of dynamic inflow modelling for rotorcraft flight mechanics. Vertica, 12(3):213–242, 1988.

[13] M. Gaunaa. Unsteady two-dimensional potential-flow model for thin variable geometry airfoil. Wind Energy, 13(2-3):167–192, 2010.

[14] Mac Gaunaa. Unsteady 2D potential-flow forces on a thin variable geometry airfoil undergoing arbitrary motion. RisøR1478(EN), 2006.

[15] J.G. Schepers H. Snel. Investigation and modelling of dynamic inflow effects. 1993.

[16] Martin O.L. Hansen. Aerodynamics of Wind Turbines. Number Ed. 3. 2015.

[17] IEC 61400-1. IEC 61400-1, Third edition. Standard, International Electrotechnical Commission, March 2005-08.

[18] R.T. Jones. Operational Treatment of the Nonuniform-Lift Theory in Airplane Dynamics, TN-667. Technical report, 1938.

[19] M. Gaunaa L. Bergami. ATEFlap Aerodynamic Model , Risø-R-Report. 2012.

[20] M. Gaunaa L. Bergami, V.A. Riziotis. Aerodynamic response of an airfoil section undergoing pitch motion and trailing edge flap deflection: a comparison of simulation methods. Wind Energy, 2014.

[21] J.G. Leishman and K.Q. Nguyen. AIAA, 28(5):836–844.

[22] Veers P.S. Lobity, D.W. Aeroelastic behavior of twist-coupled HAWT blades. AIAA, (29), 1997.

[23] M. Gaunaa M.H. Hansen and H.A. Madsen. A Beddoes-Leishman type dynamic stall model in state-space and indicial formulations. Technical report.

[24] Knudsen T. et al. Odgaaard, P.F. Combined analytical/FEA-based coupled aero structure simulation of a wind turbine with bendtwist adaptive blades. Renewable Energy, 127/503(32):916–930, 2006.

[25] Knudsen T. et al. Odgaaard, P.F. Importance of Dynamic Inflow in Model Predictive Control of Wind Turbines. IFAC, 2015.

[26] R. Damiani J. Jonkman S.A. Ning, G. Hayman. Development and validation of a new blade element momentum skewed-wake model within aerodyn. In AIAA Science and Technology Forum and Exposition. NREL, 2014.

[27] Schepers J.G. Snel, H. Joint investigation of dynamic inflow effects and implementation of an engineering method.

[28] C. Bak T. Buhl, M. Gaunaa. Potential Load Reduction Using Airfoils with Variable Trailing Edge Geometry. Journal of Solar Energy Engineering, 127/503, 2005.

[29] N. Jenkns T. Burton, D. Sharpe and E. Bossanyi. Wind Energy Handbook. 2013.

[30] T. Theodorsen. Report No. 496. General Theory of Aerodynamic Instability and the Mechanism of Flutter. NACA, 1949.

Appendix A

ATEFlap Validation Results

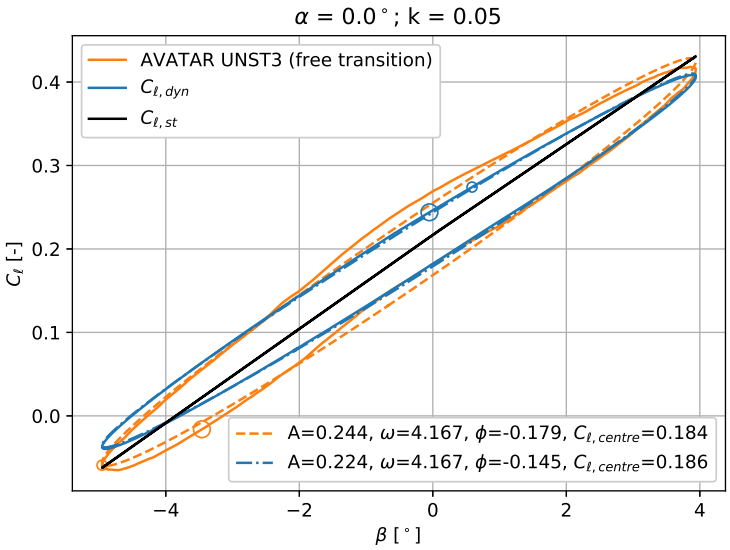

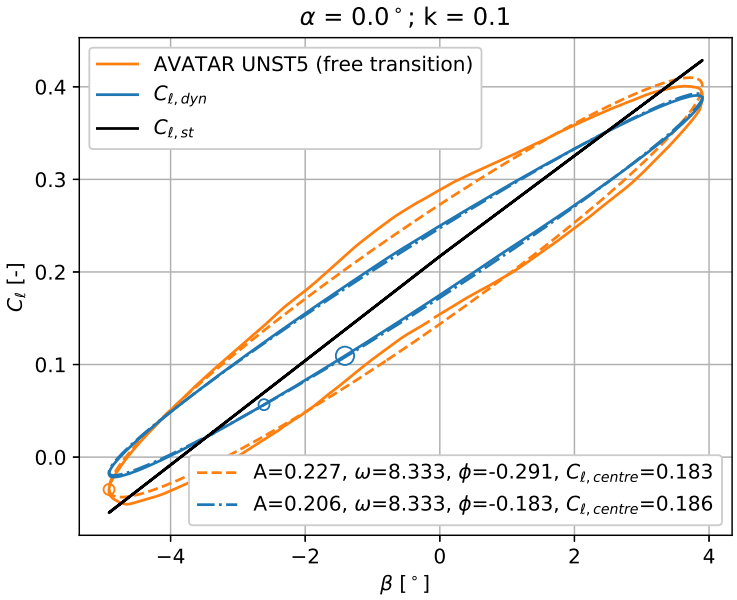

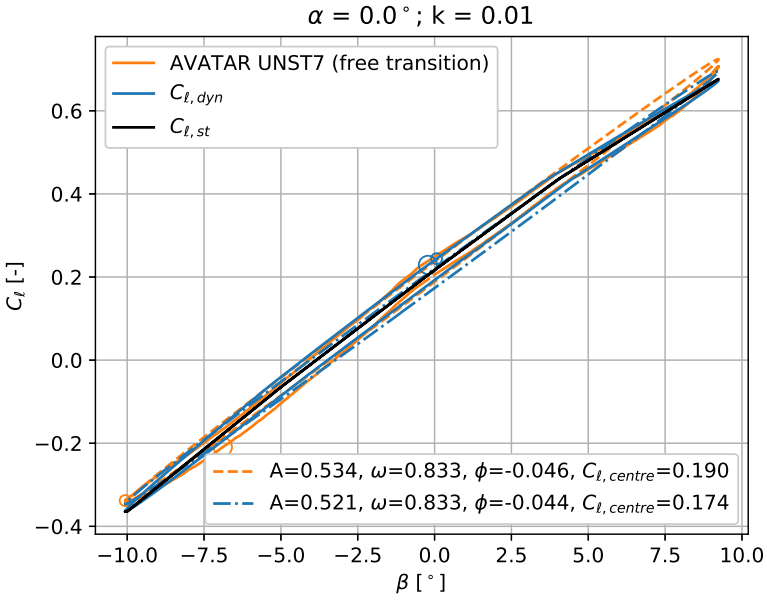

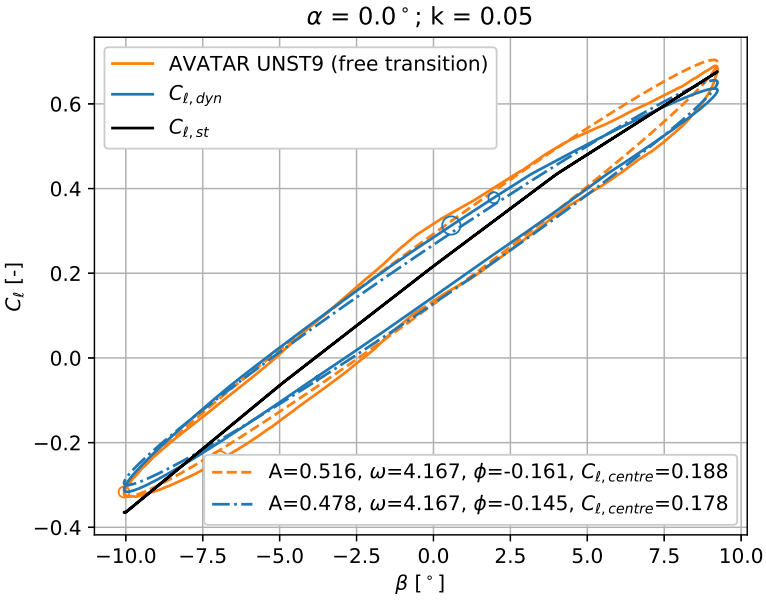
α = 0.0 ° ; k = 0.05
AVATAR UNST9 (free transition)
$C_{\ell,dyn}$
$C_{\ell,st}$
A=0.516, ω=4.167, ϕ=-0.161, $C_{\ell,centre}$=0.188
A=0.478, ω=4.167, ϕ=-0.145, $C_{\ell,centre}$=0.178
C_ℓ [-]
β [°]

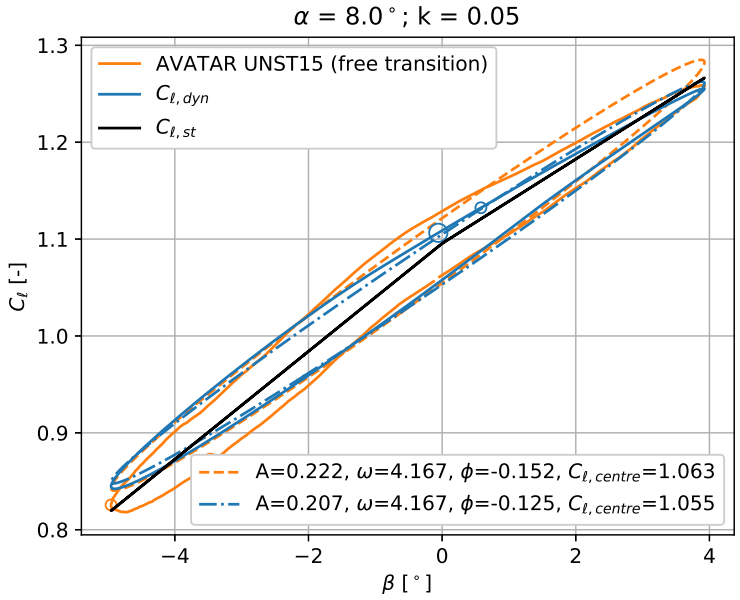
α = 8.0 ° ; k = 0.05
AVATAR UNST15 (free transition)
$C_{\ell,dyn}$
$C_{\ell,st}$
A=0.222, ω=4.167, ϕ=-0.152, $C_{\ell,centre}$=1.063
A=0.207, ω=4.167, ϕ=-0.125, $C_{\ell,centre}$=1.055
C_ℓ [-]
β [°]

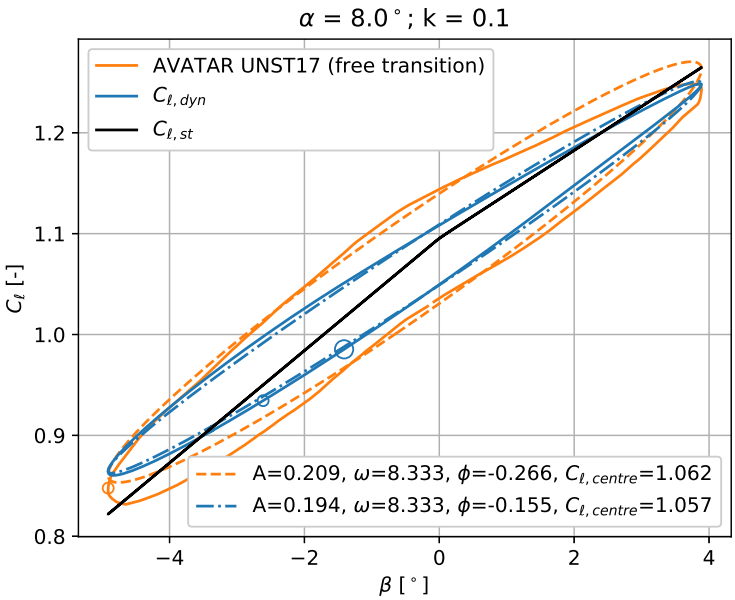
α = 8.0 ° ; k = 0.1
AVATAR UNST17 (free transition)
$C_{\ell,dyn}$
$C_{\ell,st}$
A=0.209, ω=8.333, ϕ=-0.266, $C_{\ell,centre}$=1.062
A=0.194, ω=8.333, ϕ=-0.155, $C_{\ell,centre}$=1.057
C_ℓ [-]
β [°]

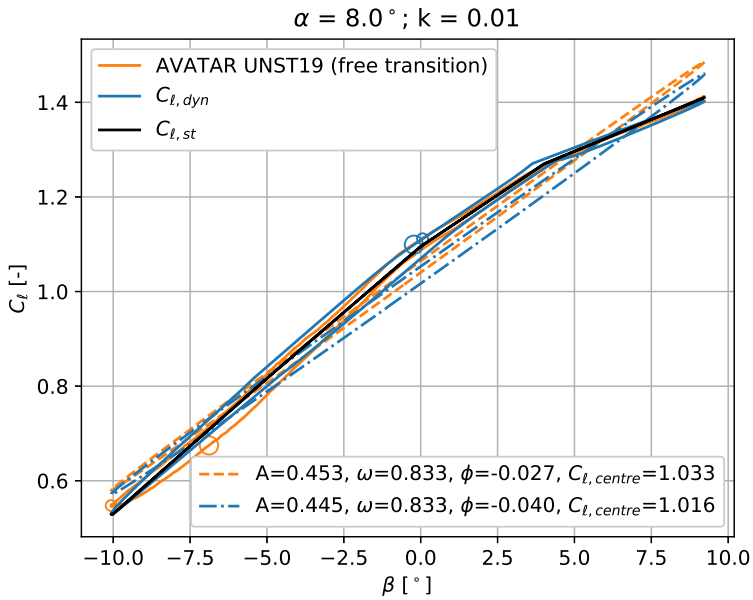
α = 8.0 ° ; k = 0.01
AVATAR UNST19 (free transition)
$C_{\ell,dyn}$
$C_{\ell,st}$
A=0.453, ω=0.833, ϕ=-0.027, $C_{\ell,centre}$=1.033
A=0.445, ω=0.833, ϕ=-0.040, $C_{\ell,centre}$=1.016
C_ℓ [-]
β [°]

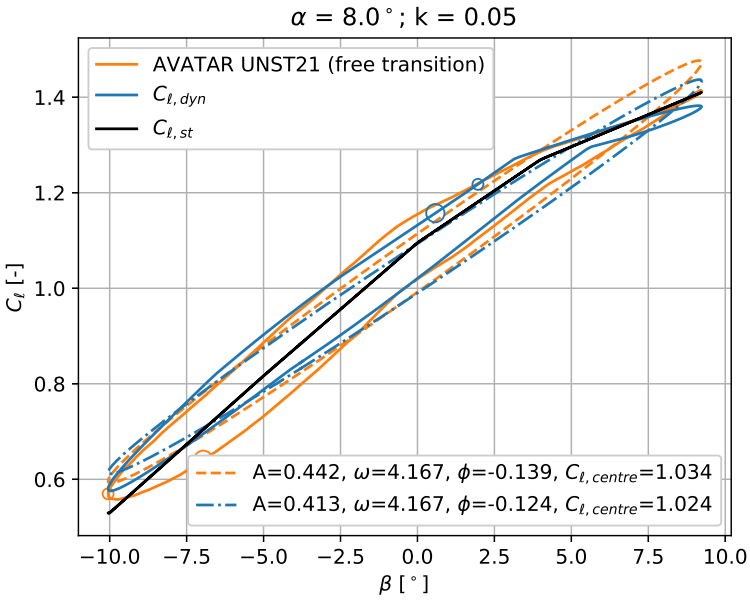
α = 8.0 ° ; k = 0.05
AVATAR UNST21 (free transition)
$C_{\ell,dyn}$
$C_{\ell,st}$
A=0.442, ω=4.167, ϕ=-0.139, $C_{\ell,centre}$=1.034
A=0.413, ω=4.167, ϕ=-0.124, $C_{\ell,centre}$=1.024
C_ℓ [-]
β [°]

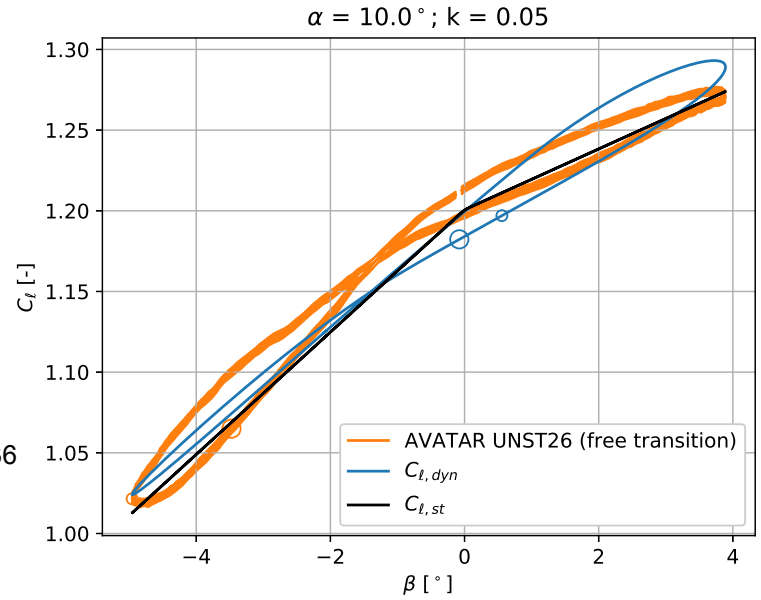
α = 10.0 ° ; k = 0.05
AVATAR UNST26 (free transition)
$C_{\ell,dyn}$
$C_{\ell,st}$
C_ℓ [-]
β [°]

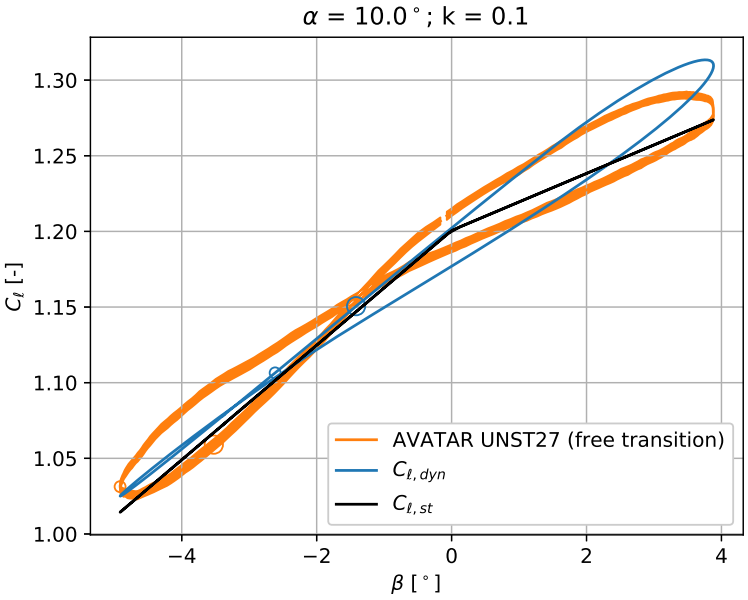
α = 10.0 ° ; k = 0.1
AVATAR UNST27 (free transition)
$C_{\ell,dyn}$
$C_{\ell,st}$
C_ℓ [-]
β [°]

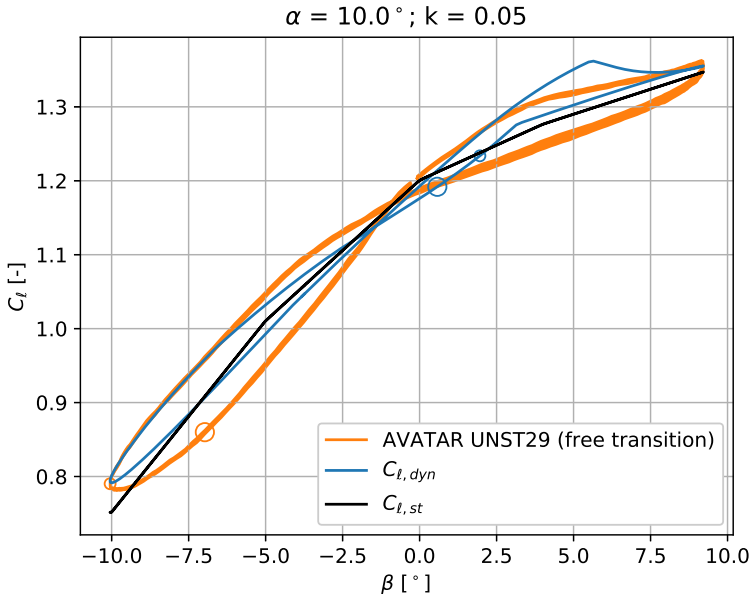
α = 10.0 ° ; k = 0.05
AVATAR UNST29 (free transition)
$C_{\ell,dyn}$
$C_{\ell,st}$
C_ℓ [-]
β [°]

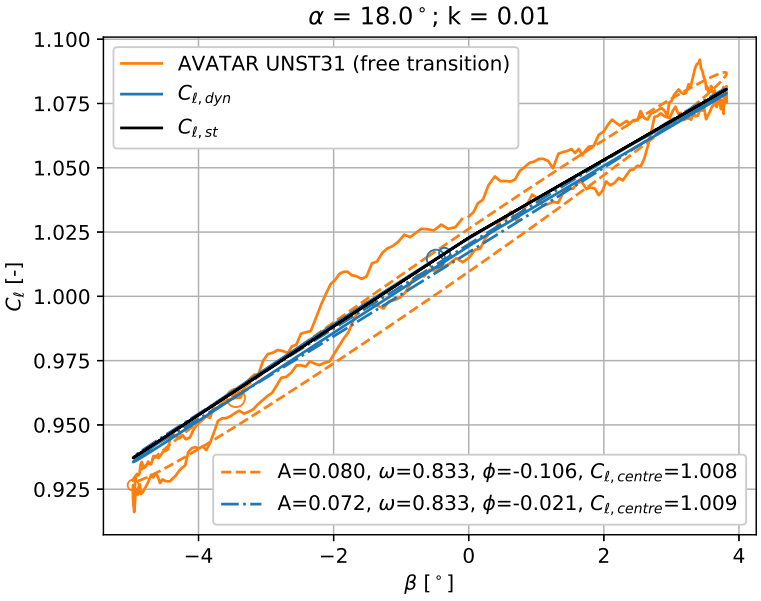
α = 18.0 ° ; k = 0.01
AVATAR UNST31 (free transition)
$C_{\ell,dyn}$
$C_{\ell,st}$
A=0.080, ω=0.833, ϕ=-0.106, $C_{\ell,centre}$=1.008
A=0.072, ω=0.833, ϕ=-0.021, $C_{\ell,centre}$=1.009
C_ℓ [-]
β [°]

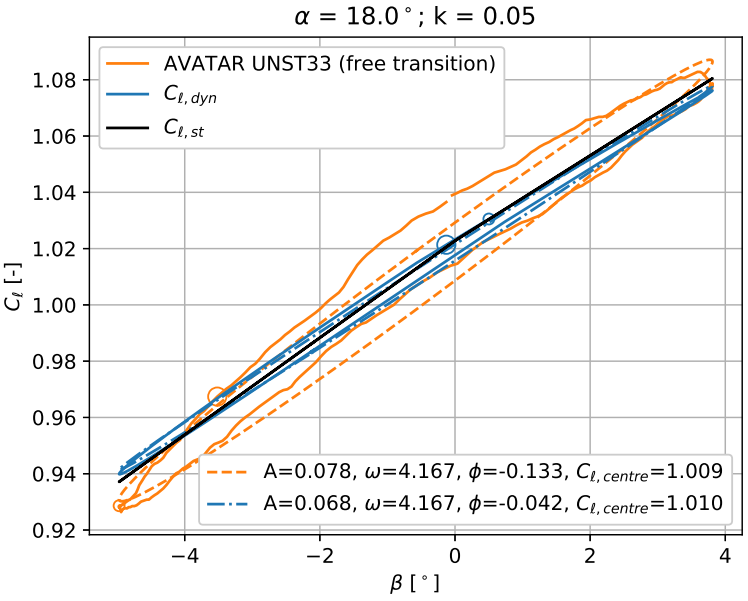
α = 18.0 ° ; k = 0.05
AVATAR UNST33 (free transition)
$C_{\ell,dyn}$
$C_{\ell,st}$
A=0.078, ω=4.167, ϕ=-0.133, $C_{\ell,centre}$=1.009
A=0.068, ω=4.167, ϕ=-0.042, $C_{\ell,centre}$=1.010
C_ℓ [-]
β [°]

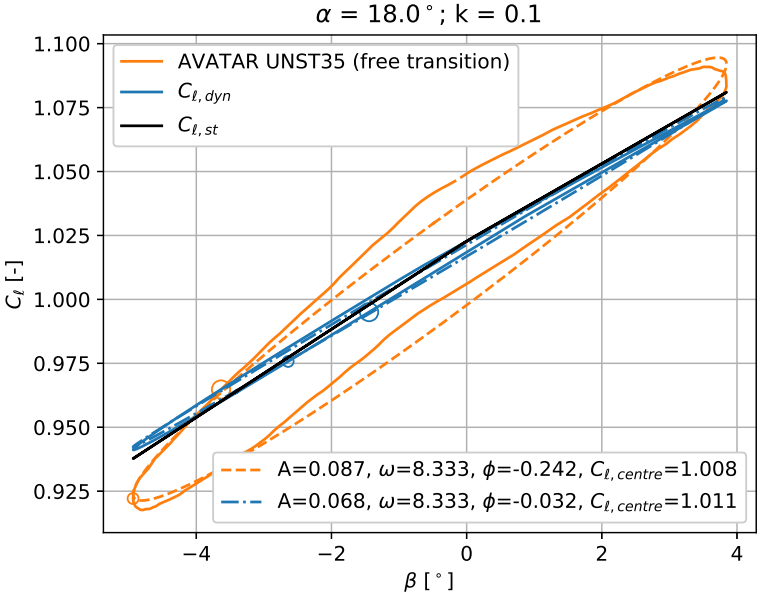
α = 18.0 ° ; k = 0.1
AVATAR UNST35 (free transition)
$C_{\ell,dyn}$
$C_{\ell,st}$
A=0.087, ω=8.333, ϕ=-0.242, $C_{\ell,centre}$=1.008
A=0.068, ω=8.333, ϕ=-0.032, $C_{\ell,centre}$=1.011
C_ℓ [-]
β [°]

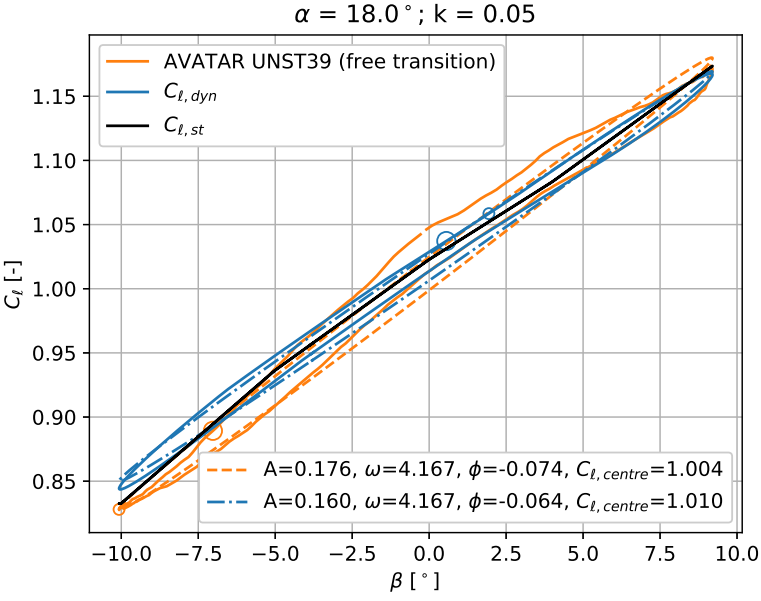
α = 18.0 ° ; k = 0.05
AVATAR UNST39 (free transition)
$C_{\ell,dyn}$
$C_{\ell,st}$
A=0.176, ω=4.167, ϕ=-0.074, $C_{\ell,centre}$=1.004
A=0.160, ω=4.167, ϕ=-0.064, $C_{\ell,centre}$=1.010
C_ℓ [-]
β [°]